Towards bright optical superchirality patterns characterized by pixel superresolution fringe metrology.

Kalff, Leander

Towards bright optical superchirality patterns characterized by pixel superresolution fringe metrology

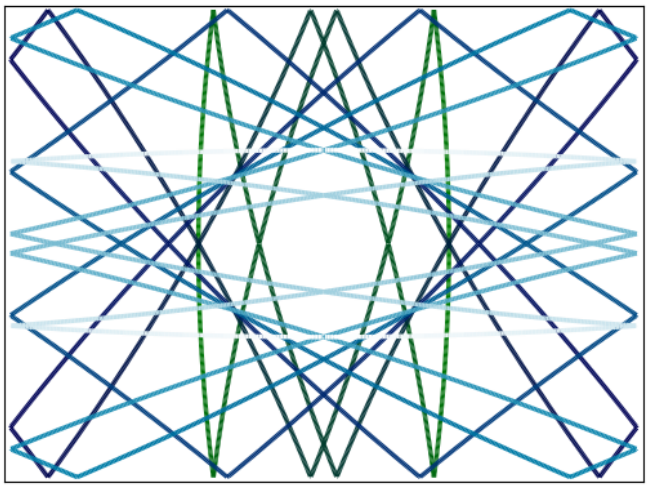

THESIS

submitted in partial fulfillment of the
requirements for the degree of

MASTER OF SCIENCE
in
PHYSICS

Author :	Leander Sebastiaan Kalff, BSc
Student ID :	s1824341
Supervisor :	Dr. W. Löffler
Second corrector :	Prof.dr. M.A.G.J. Orrit

Leiden, The Netherlands, November 10, 2023

Towards bright optical superchirality patterns characterized by pixel superresolution fringe metrology

Leander Sebastiaan Kalff, BSc

Huygens-Kamerlingh Onnes Laboratory, Leiden University
P.O. Box 9500, 2300 RA Leiden, The Netherlands

November 10, 2023

Abstract

Superchirality is a property of light with not yet fully discovered future possibilities in industry and research. In this research, an attempt to obtain a bright superchiral lattice is made by superposing four laser beams in a particular configuration. Additionally, this superposition should theoretically lead to homogeneous electric fields without modulation, which is potentially useful in microscopy. Recording the field with a simple CMOS camera and observing its fast Fourier transform gives rise to aliasing effects due to undersampling caused by the fact that interference occurs at a subpixel level. This phenomenon is investigated by numeric and analytic simulations. By rotation of the camera, pixel superresolution was achieved, which effectively enables the possibility to investigate the interference patterns at a subpixel level and hence measure the angle between pair of beams with good accuracy. With newly developed beam alignment methods we have achieved and confirmed a beam alignment that is sufficient for production of bright superchirality lattices.

Contents

Chapter 1

Introduction

Since the optical double-slit experiment of Young in 1804 [1], it is known that light behaves as a wave and therefore experiences interference upon observation. Nowadays, this behavior is broadly understood and considered undergraduate knowledge of physics. Interference of a particular kind, namely utilizing multiple laser beams, is widely used throughout multiple fields, such as, structured illumination microscopy [2], biological microscopy [3], 3D fluorescence microscopy [4], or fabrication of nanostructures using a photoresist and lithography [5, 6]. The research of this thesis is an attempt to add a chapter to the book of laser interference and the particularities involved.

In 2018, Kruining et al. [7] published a paper about the possibility of a non-trivial cancellation of the interference patterns of multiple plane waves. Non-trivial, because in three dimensions up to three beams can be put *trivially* in superposition with a homogeneous interference pattern, simply by orthogonalizing their polarizations. But for four or more beams another mathematical trick has to be applied to obtain this constant electric field intensity throughout the interference plane. One of their proposed beam configurations experiencing a vanishing interference pattern when observed, one with four beams, is investigated in this research.

Yet, the most interesting part of this configuration, is that a so-called *superchirality* lattice arises on the region of interference, meaning that regions of left-handed superchirality alternate with regions of right-handed superchirality on the scale of a wavelength. Superchiral light, first proposed by Tang & Cohen [8], is chiral light with a significantly enhanced enantioselectvity [9], the interaction of light with chiral matter. The proposed

configuration however involved *dark* superchirality, meaning that superchirality occurs at the dark spots of the field. The superchiral light that theoretically arises from the configuration of this thesis can be called *bright* superchirality, meaning that it exceeds the maximal value of the square of the electric field anywhere.

In practice, such a configuration could be useful in many fields of research involving chiral structures. The lattice can have applications in fields where the difference in chirality of matter is investigated or used. For example, metamaterials composed of chiral nanostructures can be controlled via superchiral nearfields [10], superchiral light can be used to detect the secondary structure of proteins [11] and it can be used for ultrasensitive detection and characterisation of biomolecules [12]. Recently, it has been theoretically suggested that superchiral fields can be important in circular dichroism spectroscopy and optical tweezers [13]. However, if this is helpful for detecting single-molecule circular dichroism is unclear [14], due to the weakness of the signals and influence of molecule orientation.

In this thesis it is discussed how such a field can be obtained experimentally, it is shown that some improvements are still necessary and it is argued that a small reduction of interferometric visibility was observed. Alongside this, new insights about how to use the fast Fourier transform (FFT) results in a new method to overcome aliasing and retrieve the original interference fringe distance, using the rotation of the camera [15].

First, the theoretical background to interference, superchirality and FFTs experiencing aliasing are discussed and they are provided with numerical simulations and calculations on the matter. Then, in chapter three the experimental setup is presented after which new alignment methods are developed in chapter four, leading to a quick, robust and accurate new method to determine the angle between a pair of interfering lasers. In this chapter measurements on multiple beam configurations will be analyzed, discussed and compared to simulations as well. Finally, it is argued in the conclusion that there is an indication of a vanishing interference pattern and some proposals for future research are stated.

Chapter 2

Theory & simulations

2.1 A superposition of multiple plane waves

Light, having a wave nature of itself, can give rise to interferences and this intriguing phenomenon can be observed when two coherent optical beams intersect, the interference term follows from the following electric-field intensity equations.

$$\begin{aligned} I(\mathbf{x}) \propto \mathbf{E}_{\text{tot}}(\mathbf{x})^2 = (\mathbf{E}_1(\mathbf{x}) + \mathbf{E}_2(\mathbf{x}))^2 = \\ = \mathbf{E}_1(\mathbf{x})^2 + \mathbf{E}_2(\mathbf{x})^2 + 2\mathbf{E}_1(\mathbf{x}) \cdot \mathbf{E}_2(\mathbf{x}) \end{aligned} \tag{2.1}$$

The latter term contains the information about the interference of the beams. In this thesis, the term *non-interfering* is defined as I_{tot} being homogeneous throughout the plane of interference, hence putting the term $2\mathbf{E}_1 \cdot \mathbf{E}_2$ at zero. The angle between the two beams θ (considering they have a linear polarization, both perpendicular to the wave-plane and parallel to each other) determines the spatial separation between the interference fringes, which is shown in figure 2.1 and yields $\Delta x = \frac{\lambda}{2 \sin \theta}$.

In addition to superimposing just two beams, the electric field of a system of N interfering beams at the location of interference is calculated as follows, where for mathematical reasons we change to $\tilde{\mathbf{E}}$, which is a complex electric field. The resulting intensity is already integrated over one time

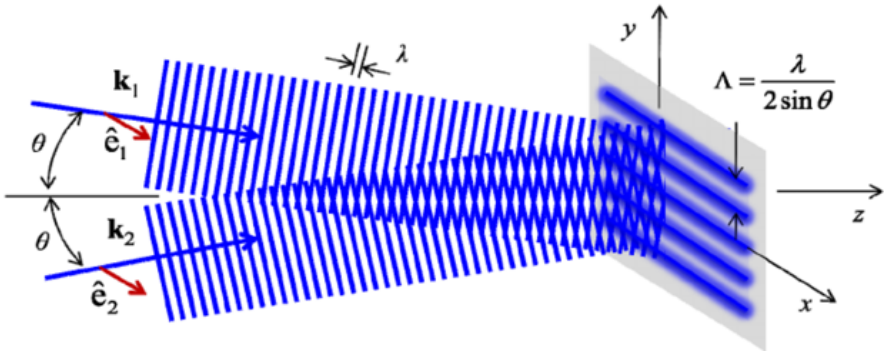

Figure 2.1: *The interference of two plane waves leads to minima and maxima in intensity separated by a typical distance of* $\Delta x = \frac{\lambda}{2\sin(\theta)}$*. This figure was obtained from Burrow et al. [16].*

period $\frac{2\pi}{\omega}$.

$$\mathbf{E} = \mathrm{Re}\left\{\tilde{\mathbf{E}}\right\} = \mathrm{Re}\left\{\sum_{j=1}^{N} \tilde{\mathbf{E}}_j e^{i\cdot\mathbf{k}_j\cdot\mathbf{x}_j}\right\} \Rightarrow$$

$$I_{\mathrm{tot}}(\mathbf{x}) = \mathbf{E}^2_{\mathrm{tot}}(\mathbf{x}) =$$

$$\frac{1}{2}\tilde{\mathbf{E}}\cdot\tilde{\mathbf{E}}^* = \frac{1}{2}\left(\sum_{j=1}^{N}\tilde{\mathbf{E}}_j\cdot\tilde{\mathbf{E}}_j^* + \sum_{j,l=1,j\neq l}^{N}\tilde{\mathbf{E}}_j\cdot\tilde{\mathbf{E}}_l^* e^{i(\mathbf{k}_j-\mathbf{k}_l)\cdot\mathbf{x}}\right) \tag{2.2}$$

The trivial solution resulting in a homogeneous interference pattern with multiple beams is when the second term equals zero due to orthogonality of the multiple beam polarizations. This can obviously only be reached when the system contains up to three interfering beams, namely when their polarization vectors are orthogonal. For more than three, there also exist (non-trivial) solutions to this problem, which is the work of Kruining et al. [7]. They have calculated non-trivial solutions from 4 up to 6 beams, where each term $\tilde{\mathbf{E}}_j\cdot\tilde{\mathbf{E}}_l^* e^{i(\mathbf{k}_j-\mathbf{k}_l)\mathbf{x}}$ is non-zero, but their sum in equation 2.2 is. A solution they have found for four beams is shown in figure 2.2. This beam configuration with $\phi = \pi/4$ is the one used in this research.

The calculation done by Kruining uses interference of plane waves, but in experiment this is not always the case, thus making this assumption not justified in every case. Laser beams are Gaussian paraxial beams, which means their divergence is very small and their intensity profile is Gaussian. Since lasers are in the paraxial regime, they can be considered to plane waves in their focal region, but with a Gaussian intensity profile.

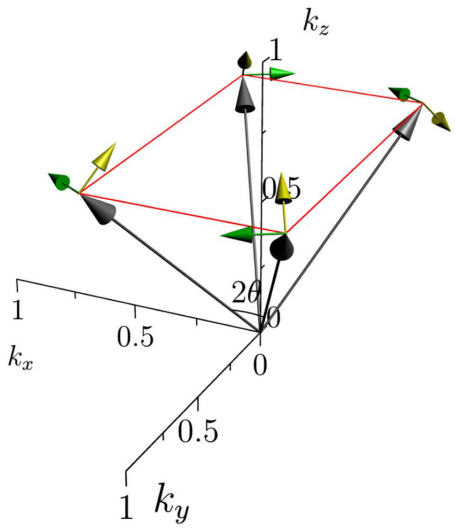

(a)

j	$\mathbf{k}_j$	$\tilde{\mathbf{E}}_\mathbf{j}$
A	$\frac{\sqrt{2}}{2}[\cos(\phi), \sin(\phi), 1]$	$\frac{\sqrt{2}}{2}a_A[-\cos(\phi), -\sin(\phi), 1]$
B	$\frac{\sqrt{2}}{2}[-\cos(\phi), \sin(\phi), 1]$	$\frac{\sqrt{2}}{2}a_B[\cos(\phi), -\sin(\phi), 1]$
C	$\frac{\sqrt{2}}{2}[-\cos(\phi), -\sin(\phi), 1]$	$\frac{\sqrt{2}}{2}a_C[-\cos(\phi), -\sin(\phi), -1]$
D	$\frac{\sqrt{2}}{2}[\cos(\phi), -\sin(\phi), 1]$	$\frac{\sqrt{2}}{2}a_D[-\cos(\phi), \sin(\phi), 1]$

(b)

Figure 2.2: *Schematic figure from Ref. [7] of the k-vectors, electric field (yellow arrow), and magnetic field (green arrow) polarizations (a) for the beam configuration investigated in this research, and their expressions (b) with the beam labels. Note, that that in panel (a), θ is a different angle than used in the rest of this thesis. In the table, ϕ is defined as the azimuthal angle around the z-axis in the x-y plane.*

2.1.1 A bright superchirality lattice

Apart from the interesting homogeneity of the interference, it turns out that also a so-called *superchirality* lattice appears in the observation plane, when the plane waves are kept in the same configuration. Superchirality is defined by Tang and Cohen [17] in 2010 and is interpreted as the light having a chirality (helicity) larger than the chirality of circular polarized light, implying that the magnetic field must play a role. Since molecules of different handedness have an absorption cross-section that depends on the chirality of the incoming light, the creation of such light can perhaps be ultimately used for separation of left and right-handed molecules in

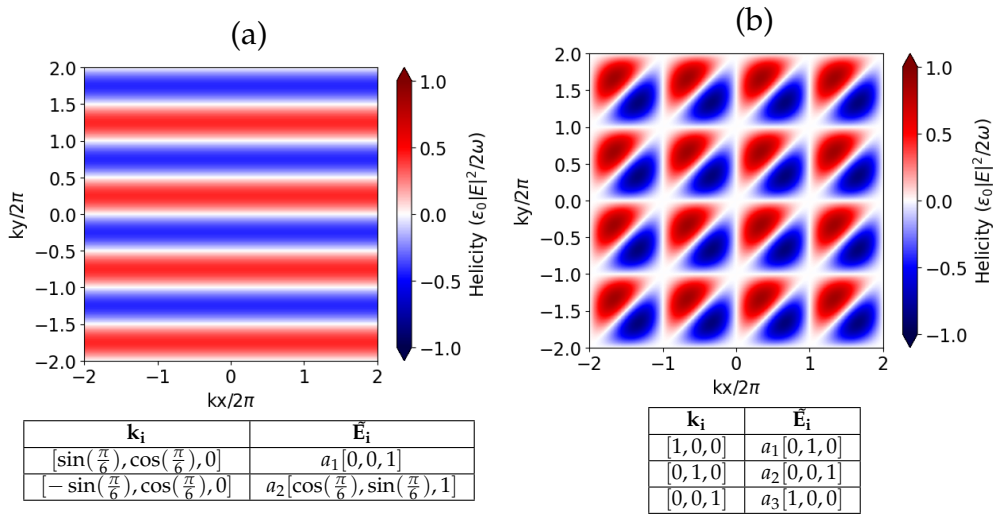

$\mathbf{k_i}$	$\tilde{\mathbf{E}}_\mathbf{i}$
$[\sin(\frac{\pi}{6}), \cos(\frac{\pi}{6}), 0]$	$a_1[0,0,1]$
$[-\sin(\frac{\pi}{6}), \cos(\frac{\pi}{6}), 0]$	$a_2[\cos(\frac{\pi}{6}), \sin(\frac{\pi}{6}), 1]$

$\mathbf{k_i}$	$\tilde{\mathbf{E}}_\mathbf{i}$
$[1,0,0]$	$a_1[0,1,0]$
$[0,1,0]$	$a_2[0,0,1]$
$[0,0,1]$	$a_3[1,0,0]$

Figure 2.3: *Plots of the helicity H for 2 (a) and 3 (b) interfering plane waves with chiral lattices that do not reach superchirality at any point in the plane of observation, but with a fully homogeneous interference patern. The axes are essentially in units of one wavelength ($\frac{x}{\lambda}$).*

chemical or pharmaceutical processes, albeit in the far future.

Helicity is a conserved quantity of the field and is introduced by Lipkin [18]. This quantity is defined as $\mathcal{H} = \frac{1}{2c\omega}\mathrm{Im}(\tilde{\mathbf{E}} \cdot \tilde{\mathbf{H}}^*)$ which for N multiple plane waves yields the following equation [7].

$$\mathcal{H} = \frac{-i}{4c\omega} \sum_{i,j=1}^{N} (\tilde{\mathbf{E}}_i \cdot \tilde{\mathbf{H}}_j^* - \tilde{\mathbf{E}}_i^* \cdot \tilde{\mathbf{H}}_j) e^{i(\mathbf{k}_i - \mathbf{k}_j)\cdot\mathbf{x}}. \tag{2.3}$$

When light is superchiral, the following inequality must hold.

$$\sqrt{\epsilon_0\mu_0}|\mathrm{Im}(\tilde{\mathbf{E}} \cdot \tilde{\mathbf{H}}^*)| > \epsilon_0 \tilde{\mathbf{E}}^* \cdot \tilde{\mathbf{E}} \tag{2.4}$$

$$\text{or } \mathcal{H} > \frac{\epsilon_0}{2}|E|^2. \tag{2.5}$$

According to Trueba & Ranada [19] helicity can also be interpreted as the difference in the number of right and left handed chiral photons: $2(N_R - N_L)$. In figure 2.3 two helicity structures are shown that arise from different input k-vectors.

When the helicity structure of the 4 input k-vectors from figure 2.2a is calculated a chirality lattice with periodicity $\frac{k}{2\pi}$ arises where the areas inside the white contour lines exceed the threshold and are thus superchiral. This superchiral lattice is shown in figure 2.4.

Version of November 10, 2023– Created November 10, 2023 - 13:12

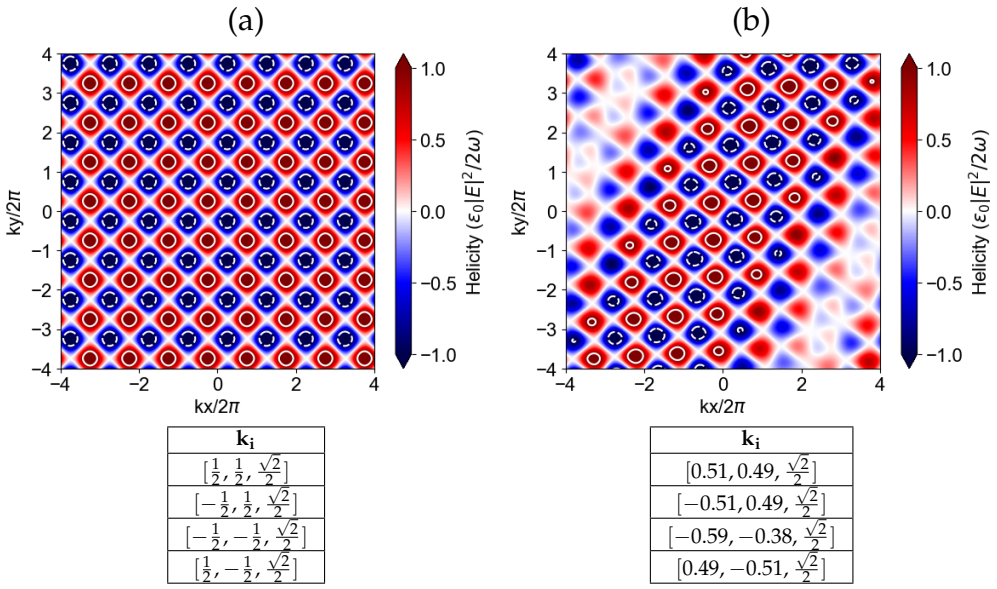

$\mathbf{k_i}$
$[\frac{1}{2}, \frac{1}{2}, \frac{\sqrt{2}}{2}]$
$[-\frac{1}{2}, \frac{1}{2}, \frac{\sqrt{2}}{2}]$
$[-\frac{1}{2}, -\frac{1}{2}, \frac{\sqrt{2}}{2}]$
$[\frac{1}{2}, -\frac{1}{2}, \frac{\sqrt{2}}{2}]$

$\mathbf{k_i}$
$[0.51, 0.49, \frac{\sqrt{2}}{2}]$
$[-0.51, 0.49, \frac{\sqrt{2}}{2}]$
$[-0.59, -0.38, \frac{\sqrt{2}}{2}]$
$[0.49, -0.51, \frac{\sqrt{2}}{2}]$

Figure 2.4: *The superchiral lattice (a) emerging from the interference of four plane waves with wave and polarization vectors similar to figure 2.2a and the lattice if the waves experience a slight azimuthal deviation (b). The white contour lines represent the locations where normal chirality reaches the superchirality threshold.*

Theoretically, it is now shown that it is possible to create a superchirality lattice with four beams. What is even more interesting, is that this superchirality is considered *bright* superchirality, which means that the spatial field satisfies $\max(\sqrt{\epsilon_0\mu_0}|\mathrm{Im}(\tilde{\mathbf{E}} \cdot \tilde{\mathbf{H}}^*)|) > \max(\epsilon_0\tilde{\mathbf{E}}^* \cdot \tilde{\mathbf{E}})$ [7]. This holds for any superchiral area in this field of view, since the interference is homogeneous. Such a field has not yet been experimentally created, to the best of our knowledge, underlining the importance of this research.

However, if beams are not well-aligned or intensities not well-matched, this structure could vanish. For example, in figure 2.4 a chiral structure with areas that do not reach the superchirality threshold is shown, caused by small azimuthal rotations of the k-vectors (and their corresponding electric fields). Whether the superchirality requirement is met can be quantified by calculating the area fraction that shows superchirality. In figure 2.5 the results of a numerical study to this is displayed. Here, the superchiral area was calculated for different input values of the plane waves. The relation between the present superchiral area and the spread in beam magnitude (I), inclination angle (θ) and azimuthal angle (ϕ) was determined by changing the input wave vectors with a randomly sampled amount,

Version of November 10, 2023– Created November 10, 2023 - 13:12

determined by the standard deviation $\sigma_{I,\theta,\phi}$, which is displayed on the x-axis.

It fully depends on the situation what fraction of superchiral area that arises from the wave configuration is considered good enough. For example, the calculation in figure 2.4(b) has its fraction of the superchiral area, denoted as the area inside the white contour lines, reduced to 7%. Still, it does show some structure. In chapter 4 it will be discussed what angular precision the setup used in this research can reach, and this analysis can help understand to what amount of superchiral area that should lead.

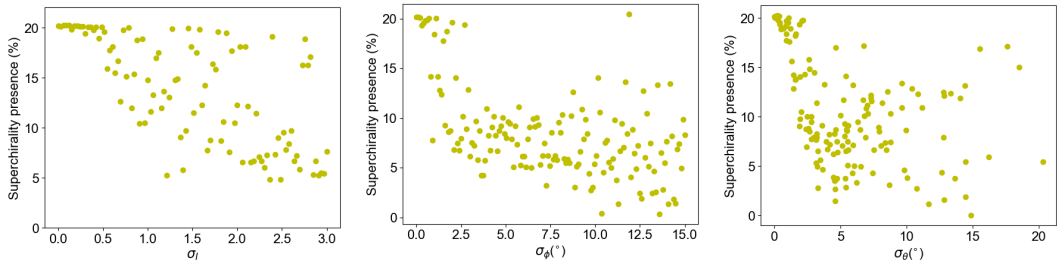

(a) ***(b)*** ***(c)***

Figure 2.5: *The influence of a deviation of different parameters of the setup on the fraction of superchiral area with respect to the total area: intensities (a), beam-angles (b) and azimuthal angles of the beams (c).*

2.1.2 The real-space interference pattern

Apart from the superchirality lattice, it is of interest to investigate the real-space interference pattern. These calculations were made using numpy [20], a package that enables handling (large) vector arrays easily. Each of the four beams the k-vector, polarization and intensity can be adjusted. Then, using the equations of sections 2.1, the interference on the virtual camera ($z = 0$) is calculated and the intensity pattern ($|E|^2$) can be calculated (figure 2.10).

In figure 2.6 three different interference patterns belonging to three configurations of beam interference are shown, all corresponding to a combination of the four beams constructed in figure 2.2. The real-space visibility is defined as $V = \frac{I_{max}-I_{min}}{I_{max}+I_{min}}$ which vanishes for a perfectly homogeneous field.

Version of November 10, 2023– Created November 10, 2023 - 13:12

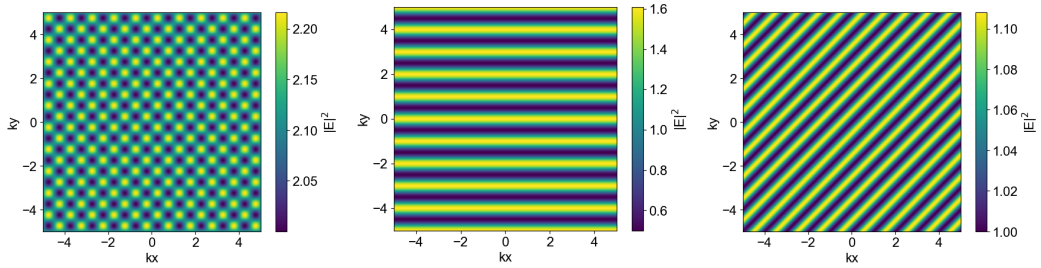

Figure 2.6: *The interference pattern of (respectively) all four interfering beams (a) two adjacent beams (b) and and two opposite beams (c)*

Now we also investigate the influence of deviations from the desired configuration on the real-space visibility. In the python simulations on four interfering beams shown in figure 2.7, the intensity, azimuth and inclination angle of the four beams are changed by a random value sampled from a normal distribution with particular standard deviation. 150 configurations were simulated and the resulting visibility is plotted as a function of the standard.

Obviously we strive to reach a perfect vanishing visibility, but for convenience for now we consider visibility below 0.1 to be of enough quality. This means that $\sigma_\theta < 0.4°$, $\sigma_\phi < 0.7°$ and $\sigma_I < 0.2$ are desired limitations to our setup. In chapter 3 & 4 it will be explained how this accuracy can be achieved.

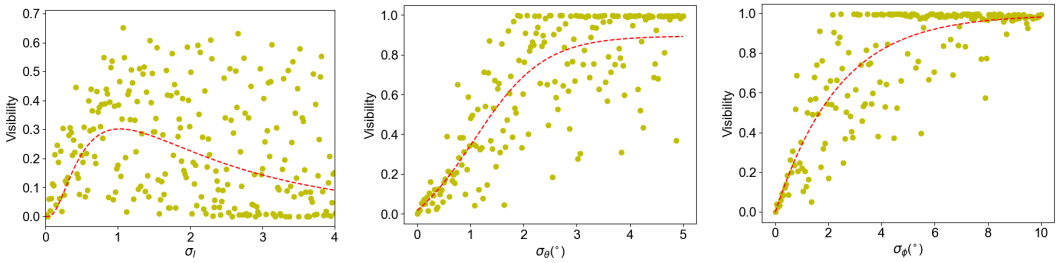

Figure 2.7: *The influence of different parameters of the setup on the measured visibility: intensity (a), beam-angle (b) and azimuth (c).*

2.2 A Fourier analysis of the interference

Since the interference pattern is a periodic structure, information about this periodicity can be visualized by the fast Fourier transform. A sinusoidal pattern will give rise to a clear peak in the frequency analysis of the FFT and it was discovered that this signal relates to the visibility of the interference fringes. Measuring the FFT peak height thus is the best method to determine whether visibility changes occur with varying beam parameters, since a real measurement of the interference fringes will be susceptible to noise which would muddle the determination of $I_{\max}$ and $I_{\min}$.

In figure 2.8 it is shown how two pairs of interfering beams give rise to certain peaks in the FFT of the obtained real-space image. From this it can be concluded that when the entire ensemble of *four* beams is observed on their region of interference, each pair of maxima corresponds to one pair of interfering beams, with the remark that a pair of FFT-peaks is one and its origin-mirrored image. Furthermore, one of the peaks arising from the fourfold interference is the center peak ($|f| = 0$) which has no information in it but the fact that this Fourier transform is a result of the discrete Fourier transform method.

To correct in this numerical simulation for the fact that the beams have a gaussian intensity profile, a kaiser filter [21] was superposed onto the pattern. This caused the horizontal and vertical lines in the FFT to disappear. In figure 2.9 it is shown how an FFT looks when the beams are in a configuration close to the theoretically perfect situation, but with slight misalignment. All beam combinations give rise to one of the peaks, and since they are misaligned, this means 4 of the previously mentioned peaks split into 2 (8 in total), since the interference patterns are not equal. From the FFT we can thus retrieve the spatial frequency, following section 2.1, making it possible to retrieve the real angle of the interfering fields via formula 2.6.

$$\theta = 2 \cdot \arcsin \frac{\lambda f_{\text{orig}}}{2} \tag{2.6}$$

Version of November 10, 2023– Created November 10, 2023 - 13:12

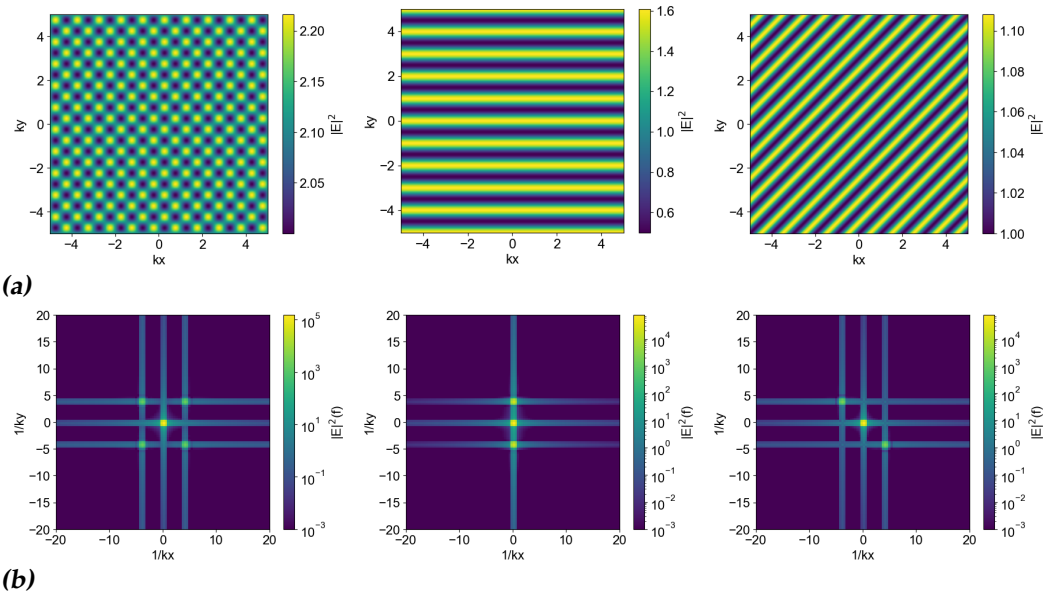

Figure 2.8: *The interference pattern (a) of respectively four interfering beams (A, B, C, D), two adjacent beams (A, C) and and two opposite beams (A, B) and their FFTs (b). The horizontal and vertical lines in (b) are due to edge effects and disappear for realistic beams.*

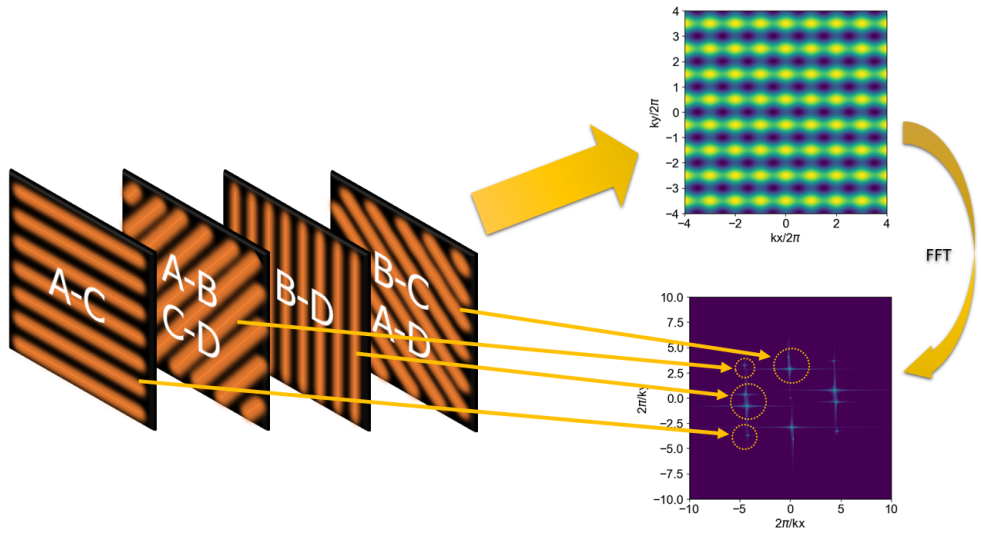

Figure 2.9: *The superposition of multiple beams can be represented as a superposition of multiple interference patterns, which all correspond to interference of a certain pair of beams.*

Version of November 10, 2023– Created November 10, 2023 - 13:12

2.2.1 Aliasing

Modifying the simulation to a more realistic situation, the effect of aliasing must be considered. Namely, in reality the interference pattern period ($\sim$ 0.23 µm) is much smaller than the camera pixel size (5.3 µm), leading to this effect. However, it was found that the FFT alias signal strength still is related to the real interferometric visibility V, so this will be investigated later on.

Because in real-space the image is heavily *undersampled*, a FFT peak analysis will lead to wrongly measured spatial frequencies. This effect is shown by simulation in figure 2.10, where the FFT peaks correspond to a frequency ($f_m \sim 0.1$ µm^{-1}) that is way to low for a beam with interference fringe distance of $\sim$ 0.23 µm and is different than what the real peak location would be ($f_{\text{original}} \sim 1$ µm^{-1}), according to figure 2.8.

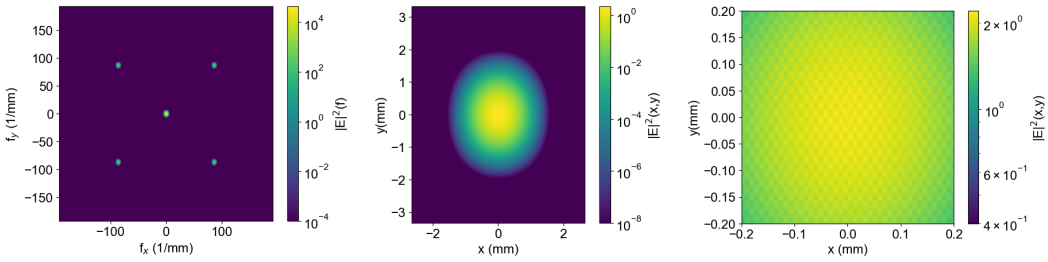

(a) ***(b)*** ***(c)***

Figure 2.10: *A numpy [20] made simulation with aliasing showing the FFT (a), the real-space (b) image with a kaiser filter and its center (c). Aliasing is implemented by averaging on* 10×10 *minipixels equally distributed over the area.*

Wan et al. [15] found out that this aliased frequency is a function of the sampling frequency (f_s) and the real frequency (f_r) and the rotation angle of the camera. In figure 2.11 it is shown how rotation of the CMOS camera effectively changes the pixel size and how this leads to walking FFT peaks. This walking-peak effect is due to the fact that, upon rotation of the camera, the size of the pixels with respect to the stationary interference fringes effectively changes size. In fact, this is not really caused by the change in size, but by the fact that (under-)sampling frequency changes, ultimately resulting in a changing Brillouin zone. Namely, when a peak crosses the edge of the Fourier transform, it passes into another Brillouin zone, which is 'folded' onto the previous one. Mathematically this leads to a relation between the measured spatial frequency f_{xm} and the sampling and real

frequency f_s and f_r yielding $f_{xm} = \left| \frac{f_r}{f_s} - \lfloor \frac{f_r}{f_s} + \frac{1}{2} \rfloor \right|$ where these L-shaped brackets represent a floor function, the function that accepts a real number as its input and yields the largest integer that is less than or equal to this number as its output.

From this knowledge a method to retrieve back the original frequency was developed involving the rotation the square pixelated camera – ideally continuously – between 0° and 90°. An entire 360°-sweep is less ideal due to practical issues, but it is also unnecessary, since the x and y coordinates of the FFT are complementary and the symmetry of the pixels can be used; they are square shaped. Any aliased FFT-peak then follows a trajectory during rotation which turns out to be uniquely dependent on the original spatial interference frequency f_{orig} (and thus the angle between the beams). Such a path is visible in figure 2.11 and could then be fitted to the model which will determine the original fringe distance. Later, in sec-

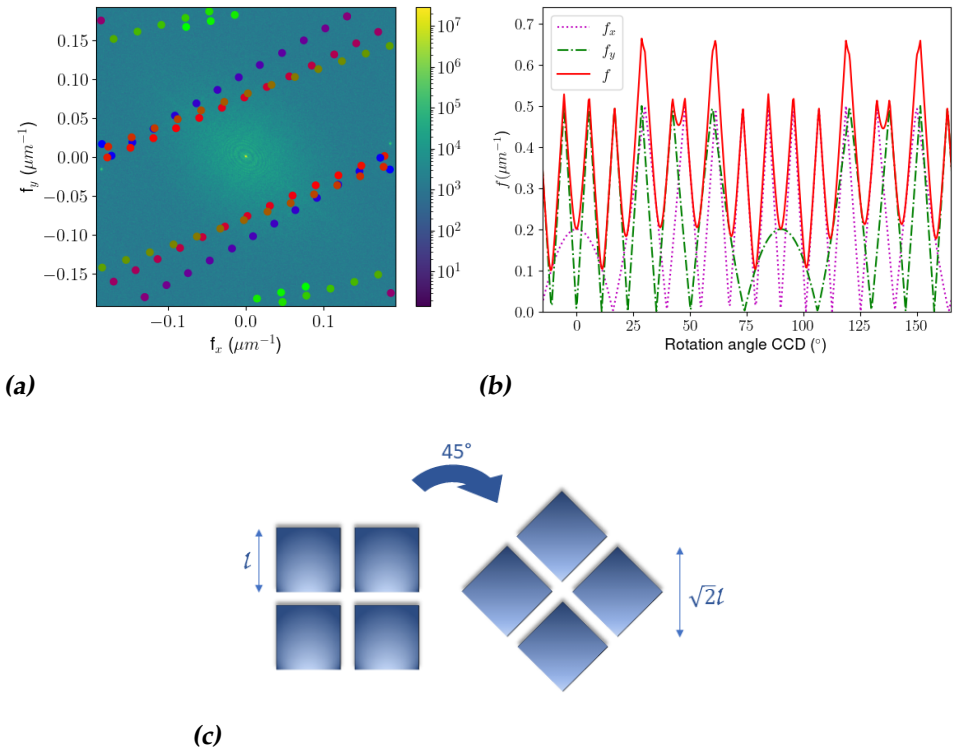

Figure 2.11: *Movement of a peak upon rotation of the CMOS camera superposed on the first frame of the measurement up to 95 frames (a) and (the x and y components of) the measured spatial frequency (b) derived from this behaviour. This behaviour can be explained by the effective change in pixel size (c).*

tion 4.1 it is shown that this knowledge can be used by fitting this model to the experimentally obtained frequencies results in a proper determination of the original beam angle.

2.2.2 Simulations on aliasing

In order to get a feeling on what implications aliasing has on our experimental results, simulations were made using a python environment before using Mathematica [22] in combination with Matlab [23]. The Python simulation consists of multiple steps, where at first – after the *real* interference field was created – a grid of (one-dimensional) points in space were sampled from this mathematically constructed electric field. This was done with the same spatial sampling frequency as the pixels in the real CMOS camera at the point of interference.

However, rotating the field with respect to the camera in simulation leads to different behavior than the model predicted. Particularly, the FFT peaks did not travel in a clear path but hopped around the spatial-frequency space. This behavior is represented by the x-coordinate of the measured spatial frequency f_{xm} in figure 2.12. The y-component showed similar behavior.

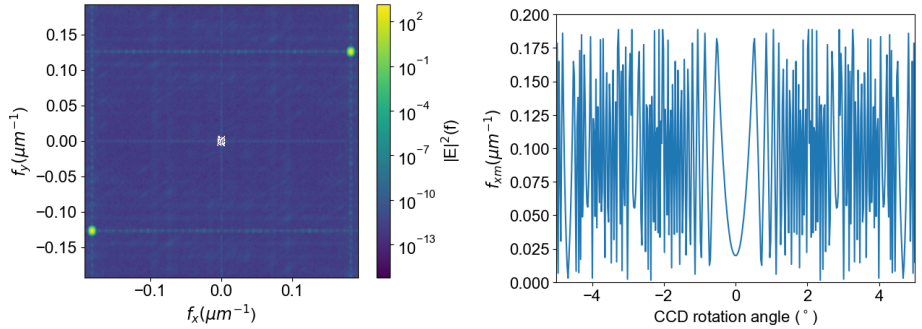

Figure 2.12: *A numerical simulation showing the FFT on a certain rotational angle of the simulated CCD (a) were the maximum at $|f| = 0$ was deleted from the image to improve the analysis. The measured spatial frequency with respect to the rotational angle of the CCD (b) shows interesting behavior when measuring with angular stepsizes below 0.05°.*

This intriguing behavior can be explained by the fact that only a one-dimensional point is sampled while in fact a continuous integral of the field on the pixel is performed, leading to a continuously changing aliasing effect while rotating. Intuitively this is hard to grasp, since one frame of the rotation seems to show normal aliasing. But, given the fact that a pixel integrates over an entire area and that in simulation the aliased signal is determined by the location of just one point, it is understandable

Version of November 10, 2023– Created November 10, 2023 - 13:12

that rotation has a much larger effect on the single one-dimensional point and thus the alias, than on an area which is averaged on.

To overcome this problem, an averaging method was tried using a square array of so-called *minipixels* at the region of a *real* pixel, over which is averaged. Numbers ranging from 4×4 up to 10×10 were investigated. Nonetheless, this made the datasets necessary for research very large, and the discontinuous hopping behaviour remained even when the simulated CCD rotation angle resolution was increased significantly. There even seemed to be no improvement when increasing the amount of minipixels. If figure 2.13 the FFT peak location and height as a function of simulated CCD rotation angle is displayed.

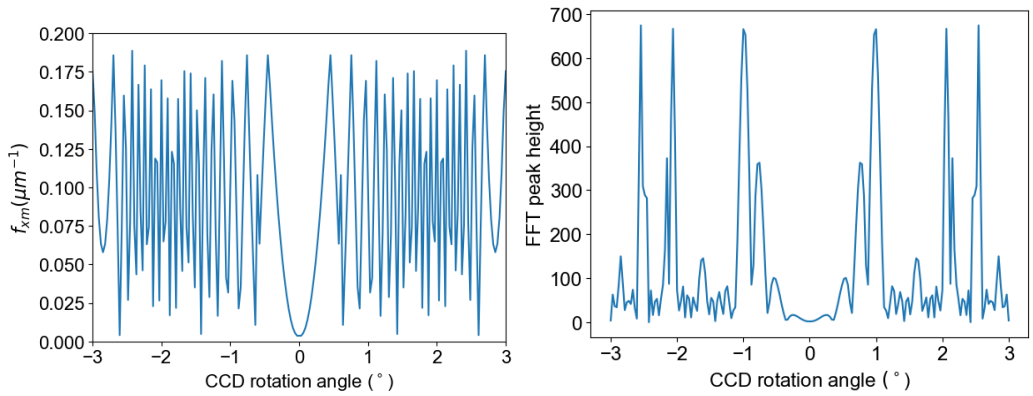

(a) ***(b)***

Figure 2.13: *The x-component of the measured (aliased) spatial frequency (a) as a function of the rotation angle of the simulated CCD and the corresponding FFT peak heights (b). In this simulation over* 5×5 *minipixels was averaged.*

2.2.3 A different approach using Mathematica

With this effect being too persistent, another approach to the simulation was investigated. The program Mathematica [22] was used in order to analytically solve the electric field at the area of interference with a proper gaussian envelope simulating the gaussian beam interference. This equation was then used in Matlab [23] to calculate the FFT for CCD rotation angles between 0 and 180°.

Mathematica is able to solve analytically hard problems if good enough boundary conditions are given. Therefore in this simulation only interfer-

Version of November 10, 2023– Created November 10, 2023 - 13:12

ence of two beams is investigated, reducing the computational toughness. The interference of two beams can still give a good insight on the influence of parameter changes like alignment or intensity. The two waves were constructed as follows.

$$\tilde{\mathbf{E}}_A = \tilde{\mathbf{E}}_B = \begin{bmatrix} 0 \\ 1 \\ 0 \end{bmatrix}$$
$$\tilde{\mathbf{k}}_A = \begin{bmatrix} \sin(\theta_A) \\ 0 \\ \cos(\theta_A) \end{bmatrix}, \tilde{\mathbf{k}}_B = \begin{bmatrix} \sin(-\theta_B) \\ 0 \\ -\cos(\theta_B) \end{bmatrix}$$

Then, a rotation with angle θ_{pol} of the polarization around the **k**-vectors of the separate plane waves was made, in order to be able to measure maximal interference (parallel, $\theta_{\text{pol}} = 0°$) and zero interference (orthogonal, $\theta_{\text{pol}} = 90°$). This configuration is shown in figure 2.14. Furthermore, the possibility of rotating all beams along the z-axis with an angle θ_{rot} was put in with a simple rotation matrix. Next, equation 2.2 was used to compute the intensity at the right place depending on parameters. Lastly, the CCD grid was made, which allowed Mathematica to integrate over the pixel distance of 5.3 µm. This problem was only solvable if either θ_A and θ_B were put to $\frac{\pi}{4}$ or θ_{pol} was given a certain value. This allowed us to investigate and compare the FFTs for cases with presumed high and low interference amounts and investigate the influence of the pixel size with respect to the scale of the interference pattern. All FFTs were created with the condition of $0 \leq \theta_{\text{rot}} \leq \pi$.

Subsequently, the generated FFTs could be analyzed by the same python algorithm as in the previous section. From this, the relation of f_x, f_y and the FFT peak height to the CCD angle could be found. They are displayed in figure 2.15 and are closer to reality, because the discrete nature of the first simulation was eliminated using Mathematica. Furthermore, the shape of f_{xm} in figure 2.15a is similar to the shape in figure 2.11b and hence this method can be considered correct and accurate. Even the amount of *folds* is equal to the experimental case, which will be elaborated on later.

2.2.4 An analysis of the simulations

At first, two beams were simulated with parallel polarization and compared to when these two beams have the same angle ($\theta_{BD} = 90°$), but

Version of November 10, 2023– Created November 10, 2023 - 13:12

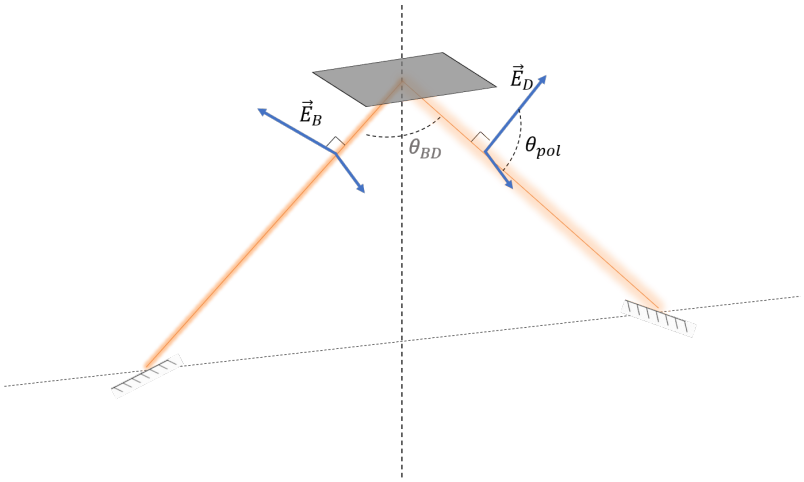

Figure 2.14: *A representation of the simulated configuration of two interfering beams with tunable parameters θ_{pol}, θ_{BD} and intensity.*

with two polarizations that are near-orthogonal to each other ($\theta_{\text{pol}} = 90°$). In figure 2.15b the result of different rotation angles is shown and it becomes immediately obvious that all the curves are similar up to a scaling factor. Now consider the equation of the field at the region of interference, for polarization angle of the beams for two beams at $\theta_{\text{pol}} = 90°$ and with Δx the pixel distance, calculated by mathematica.

$$\int_{x_0}^{x_0+\Delta x}\int_{y_0}^{y_0+\Delta y} |\tilde{\mathbf{E}}|^2 \,|_{z=0}\, dxdy = \frac{1}{2}(E_B^2 + E_D^2)\Delta x^2 \tag{2.7}$$

$$+\frac{1}{2}E_B E_D \cos^2(\theta_{pol})\csc(\theta_{CCD})\sec(\theta_{CCD})\cdot \tag{2.8}$$

$$\cdot\Bigg(\cos\left(\sqrt{2}(x_0\cos\theta_{CCD} + (\Delta y + y_0)\sin\theta_{CCD})\right)$$

$$-\cos\left(\sqrt{2}((\Delta x + x_0)\cos\theta_{CCD} + (\Delta y + y_0)\sin\theta_{CCD})\right)$$

$$-2\sin\left(\frac{\Delta x\cos\theta_{CCD}}{\sqrt{2}}\right)\sin\left(\frac{(\Delta x + 2x_0)\cos\theta_{CCD} + 2y_0\sin\theta_{CCD}}{\sqrt{2}}\right)\Bigg).$$

This explains why the shape is contained when altering the polarization direction; only the second term with $\cos^2(\theta_{\text{pol}})$ is dependent on θ_{pol} and hence determines the magnitude of the interference part of the two beams, which can be recognized by the two amplitudes of the different fields E_A and E_C.

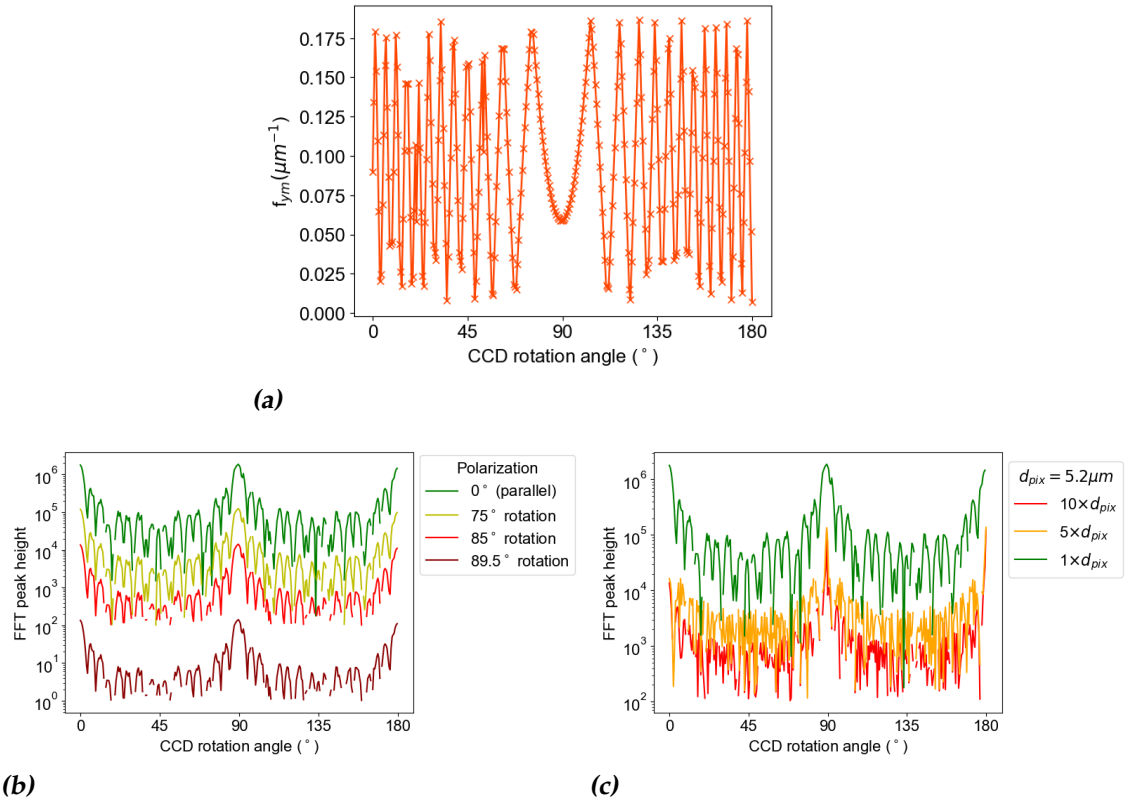

Figure 2.15: *The y-component of the measured spatial frequency (a) and the height of the FFT peak of the interference of two beams with $\theta_{BD} = 90°$ with different polarization directions (b), different intensity ratios of the two beams with $\theta_{pol} = 85°$ (c) and different pixel sizes with parallel polarized beams (d).*

Note, that in these figures some data points vanish. This discontinuity is due to the fact that the peak finding method does not perform well enough and hence these data points are mostly deleted through a check whether they cross a certain threshold. Still, the general shape is to be trusted even at low FFT peak heights, although this up and down pattern is presumably suppressed by other effects at this scale.

For example, the FFT peak height maximum around 0°, 90° etc. is due to the fact that at this angle undersampling is lowest due to the effective pixel size, so the FFT 'collects' most information about the interference pattern in the peak at this point. The minimum is accordingly at $45°(+n \cdot 90°)$, where undersampling is highest, i.e. the pixel is effectively the largest, compared to the fringe distance.

Secondly, it was examined whether the size of the pixels had an influence

on the shape, which hypothetically should have a large influence, due to a changing sampling frequency Figure 2.15c confirms this hypothesis. With an increasing pixel size, the alias strength increases leading to an increased amount of 'folds', the behavior of FFT peaks traveling into the next Brillouin zone while rotating. This also makes the peak finder algorithm less effective. It also confirms the intuitive explanation that the change of the effective size of the pixel through rotation causes the variation in the FFT peak height. When decreasing the pixel size, the peak finding analysis was not reliable anymore so this was not displayed. Still, it was clear that the amount of folds in the measurement of the (aliased) frequency decreased, confirming that the pattern of the measured frequency is uniquely dependent on the ratio between the sampling frequency and the real frequency.

In conclusion, these simulations give an insight in the behavior of the FFT peaks and predict at first that the height of the FFT peaks can be used as a measure for the amount of interference and moreover, that the peak around a CCD rotation angle of 0° ($+n \cdot 90^\circ$ with n any integer) can be examined best to properly determine a difference in the amount of interference in experiment.

Version of November 10, 2023– Created November 10, 2023 - 13:12

Chapter 3

Experimental methods & materials

In figure 3.2 the setup is shown that installs the beams in the desired configuration and polarization. A Helium-Neon is used from the company Uniphase [24] with a wavelength of 632.8 nm. Important to note about this setup is that it includes an approximately equal path length for each split beam to retain coherence at the region of interference. Figure 3.1 shows how the beams in practice are directed upward to the CMOS camera.

The filters in the setup are used to make sure the pixels in the camera do not get saturated and the beams are of equal intensity when reaching the camera. The half-wave plate allows us to switch between parallel and orthogonal polarization of all optical beams.

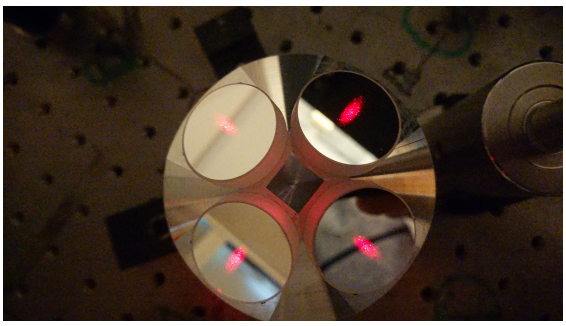

Figure 3.1: *The FMD-made mirror mount that directs the beams towards the CMOS camera.*

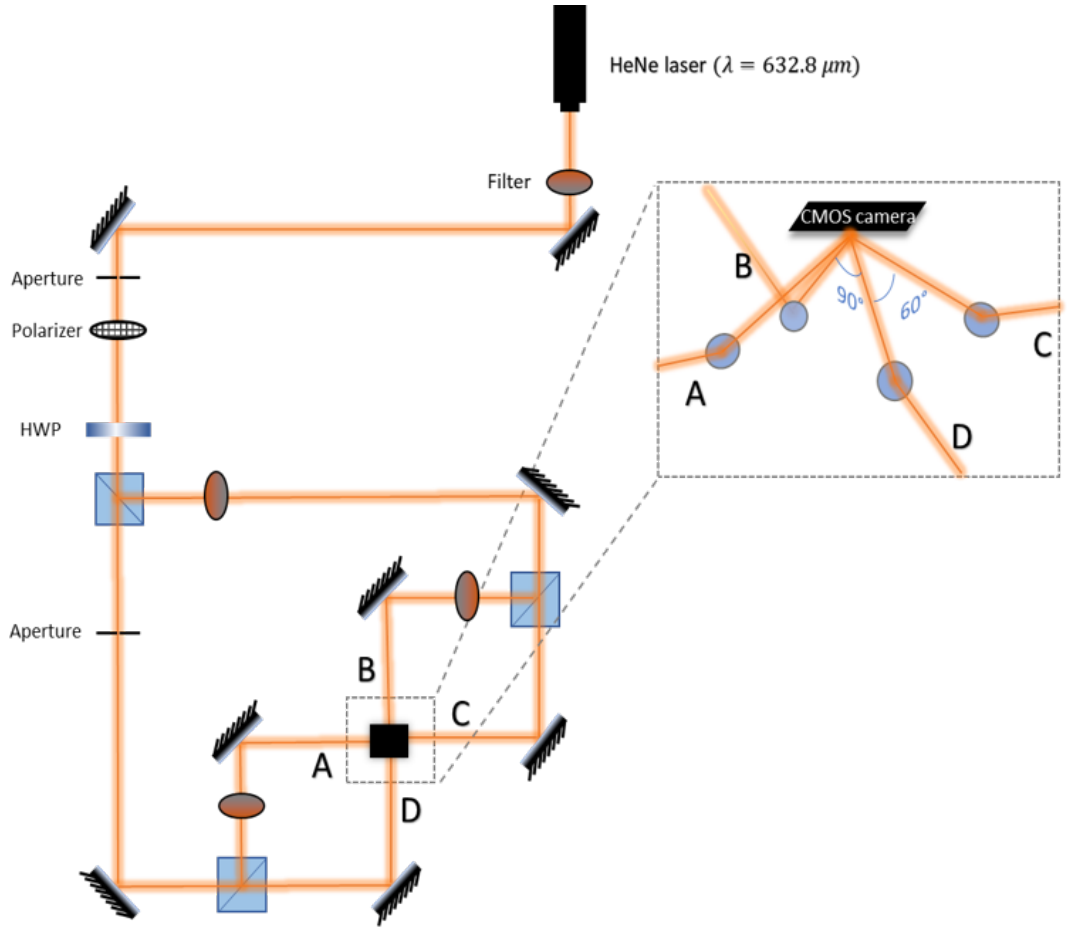

Figure 3.2: *A schematic representation of the optical setup used in this research. The entire setup can be considered 2D, except near the CMOS, as is made visible in the close up. Here, the beams are directed upwards with a desired angle of 45° with respect to the vertical axis.*

Polarizer

The polarizer used in the setup is a Thorlabs GT5-A polarizer [25] made of calcite which has an extinction ratio of 10^5 : 1 and essentially is a polarizing beam splitter. The s-polarized light is reflected off the edge of the two parts of the polarizer and directed outward, which is known as a Glan-Taylor polarizer. In the setup used in this research this beam is absorbed by the surrounding mount. In the wavelength region between 350 nm and 2.3 µm it functions best. The polarization control by this polarizer is considered enough to be suitable for the experiment.

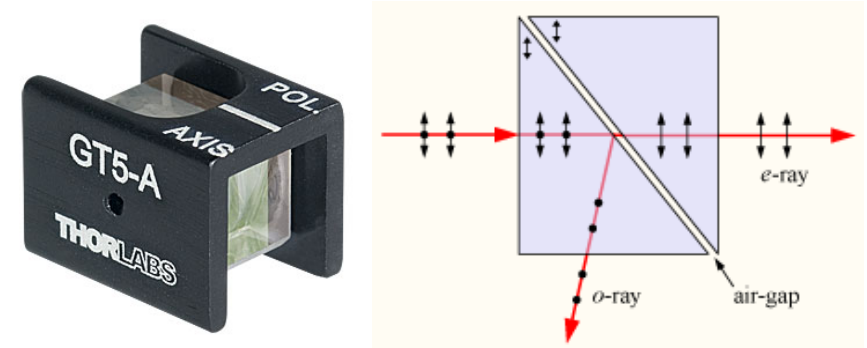

(a) *(b)*

Figure 3.3: *The Glan-Taylor polarizer (a) that is used in the setup to define the polarization of the beams and a schematic figure about how the polarizer functions (b).*

CMOS and its motion control

The CMOS-1201 Nano [26] camera has 1280×1024 pixels (1.3MPixel) with size 5.3 µm × 5.3 µm and it was attached to a stage that could maneuver it in the z-direction and was placed into a mount that was able to be rotated around its axis. This motion was controlled by the Newport ESP301 Motion Controller [27] and is according to the manufacturer very precise at small steps.

Object	Producer	Purpose	Properties
HeNe Laser [24]	Uniphase	Experiment	λ =632.8 nm
Polarizer [25]	Thorlabs	Experiment	Glan-Taylor polarizer
CMOS [26]	Cinogy	Image the intensity profile	1024×1280 pixels of 5.3µm× 5.3µm
ESP301 [27]	Newport	CMOS rotation	
Beamsplitter [28]	Thorlabs	Experiment	
Power meter [29]	Thorlabs	Intensity measurement	
HeNe Laser [24]	Uniphase	Alignment of reticle	
Half-wave plates [30]	Thorlabs	Polarization rotation	
Piezo amplifier [31]	Physik Instruments	Relative phase confinement	

Table 3.1: *The specifications of the materials used in the experiments.*

Chapter 4

Results & discussion

4.1 A new alignment procedure

In order to achieve the theoretically predicted superchirality lattice and an observable decrease in interferometric visibility of the four combined lasers an appropriate alignment procedure was developed. In the first stages of this process, a measurement of the angles of the beams was performed by projecting the beams on the wall and performing a measurement of the distances to the supposed region of interference hence measuring the relative angles. The measured azimuthal and inclination angles between the beams are displayed in table 4.1.

i	ϕ_i	θ_i
A	$93^\circ \pm 1.5^\circ$	$45.3^\circ \pm 0.9^\circ$
B	$184^\circ \pm 1.7^\circ$	$46.1^\circ \pm 1.0^\circ$
C	$263^\circ \pm 0.4^\circ$	$44.1^\circ \pm 0.9^\circ$
D	$0^\circ \pm 0.5^\circ$	$45.2^\circ \pm 1.5^\circ$

Table 4.1: *The azimuthal and inclination angles of the laser beams measured by projecting them on the ceiling and the wall. The errors of these angles were calculated using the principle of propagation of uncertainty, assuming the distance measurement error to be around* 5 *cm at long distances (*$>$ 100 *cm) and* 0.5 *cm at small distances (*$\sim$ 10 *cm).*

A perfectly homogeneous interference pattern was not observed when measuring these beams, due to their misalignment. This was observed by looking at the FFT. This is in agreement with chapter 2 and we con-

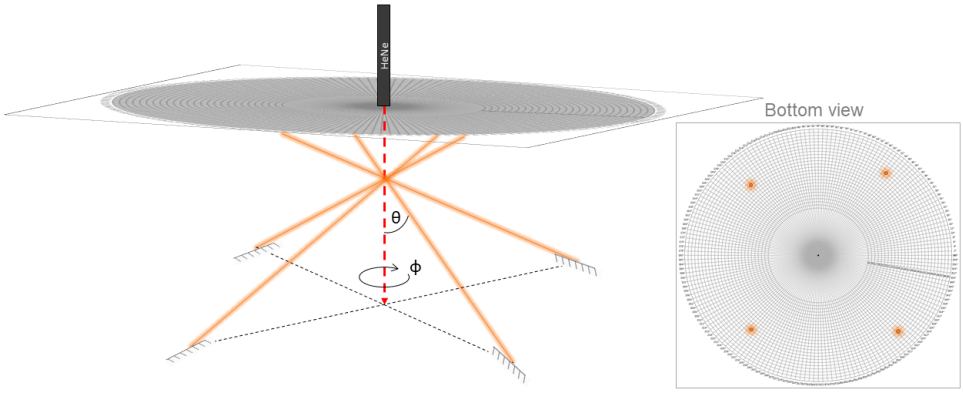

Figure 4.1: *A schematic view of the setup where the reticle was used to determine (in polar coordinates) the direction of the beam while keeping them intersecting.*

cluded that the alignment is not sufficient for a homogeneous interference pattern. Thus, a drastic improvement was made to manually improve the configuration, mainly by eye.

4.1.1 Manual and visual methods for alignment analysis

First, in order to obtain a better precision, a board with a precise reticle with a radial line at every 2° and a circle every 8 mm was made. A laser was attached to the back of the board in order to align it with the center of the mirror mount directing the beams upwards. These mirrors direct the beams towards the camera which should be placed on the location of interference, but are for the sake of alignment targeted onto a semitransparent glass plate which is used to check if the beams share the same center and if the separate beams reach the reticle. This setup is schematically shown in figure 4.1 and allowed us to investigate the θ and ϕ angles of the lasers.

Since the beams have an angle of approximately 45° with the reticle, the height is chosen to be around 30 cm in order to have an equally sized radius of circle of projection of the spots on the reticle. The accuracy such a board can include to the setup can be calculated and turns out to be equal to $s_\theta = \frac{1}{h(1+\tan^2(\theta))}\sqrt{s_x^2 + \tan^2(\theta)s_h^2}$, which results in a precision of 0.13° for a height of 30 cm, a desired $\theta = 45°$ and a spatial precision of the position

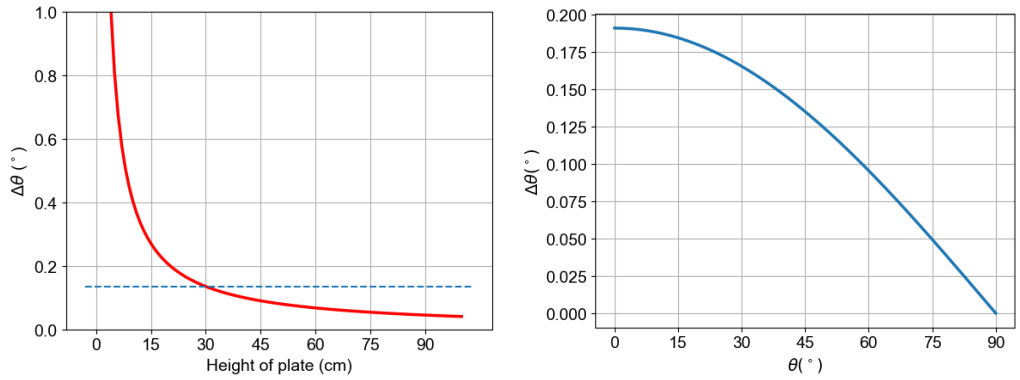

(a) ***(b)***

Figure 4.2: *The uncertainty in the angle between the beam and the z-axis with respect to the desired angle (a) and the height of the reticle board above the setup (b).*

of the board of 1 mm. The relation between $\Delta\theta$ and respectively θ itself and the height of the board is shown in figure 4.2. This precision is considered close enough to the desired angle for this experiment and this method is hence used to put the beams in proper alignment *before* measurement.

In addition to this physical alignment enhancement *before* using the camera, the real time FFT of the image – as was mentioned in section 2.2 – can play a role in enhancing the quality of alignment by eye. Namely, if the FFT peaks are in a perfect square (shown in figure 4.3), then the next statement following from straightforward trigonometry holds: $f_{\text{vertex}} = \sqrt{2} \cdot f_{\text{edge}}$, where f represents the absolute distance of the peak to the origin in reciprocal space. From section 2.1 we obtain the relation* between beam-angle and interference period $\theta = 2 \cdot \arcsin \frac{\lambda \cdot f}{2}$, therefore we can obtain a relation between the angle between *opposing* (corner peaks in the FFT) beams and the angle between *adjacent* (edge peaks in the FFT) beams

*In this relation θ represents the angle between the beams, not the polar coordinates of the FFT peaks in reciprocal space.

Version of November 10, 2023– Created November 10, 2023 - 13:12

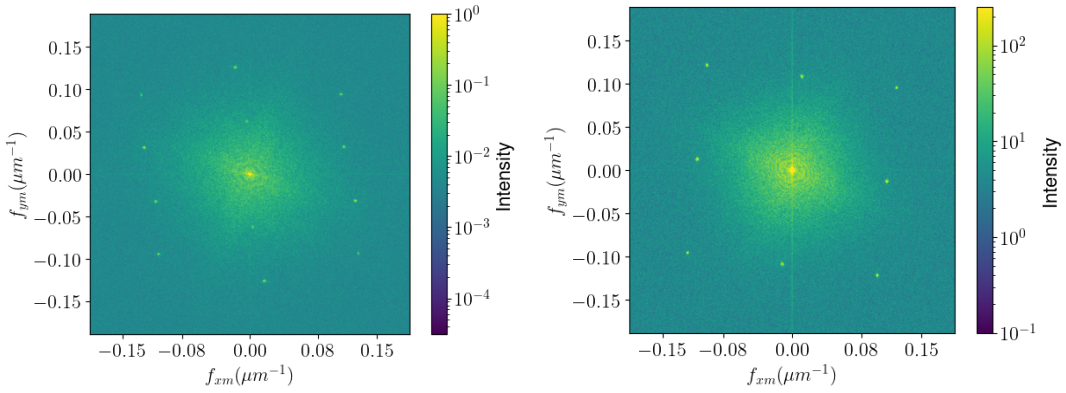

(a) ***(b)***

Figure 4.3: *FFT of four not well-aligned beams where the adjacent-interference maxima do not overlap (a) and an FFT of four beams in superposition in almost a perfect square with the adjacent-interference maxima overlap (b).*

which confirms the fact that they must be in a perfect square.

$$\begin{aligned}
\theta_{\text{corner}} &= 2 \cdot \arcsin(\lambda \frac{f_{\text{vertex}}}{2}) \\
\theta_{\text{corner}} &= 2 \cdot \arcsin(\sqrt{2}\lambda \frac{f_{\text{edge}}}{2}) \\
\theta_{\text{corner}} &= 2 \cdot \arcsin(\sqrt{2} \sin \frac{\theta_{\text{edge}}}{2}) \\
\Rightarrow \theta_{\text{corner}} &= 2 \cdot \arcsin(\sqrt{2} \sin 30°) = 90°.
\end{aligned}$$

Note, that this relation changes upon aliasing, because aliasing does not influence the general shape of the FFT. Furthermore, the FFT-peak corresponding to the interference of two adjacent beams (for example A & B) must overlap exactly with the FFT-peak of the two opposing adjacent beams (for example C & D) if they are equally aligned, because their interference patterns should have the same frequency and direction. This allows us to achieve near-perfect alignment, since it couples two beam combinations together and couples the information about the adjacent beam interference to the opposing beam interference, hence reducing the amount of free parameters.

To conclude, by keeping the beams concentric in the real-space image, making the adjacent beam interference peaks overlap and roughly making sure the peaks are in a perfect square, a better alignment quality could be reached just by looking at the live FFT of the interfering beams.

4.1.2 Precise angle determination by FFTs

To further improve the knowledge about the angle between the beams, a new automated procedure is implemented. We have seen in chapter 2 that when the camera rotates, the FFT maxima move around in spatial-frequency space. Such a trajectory is unique for the real spatial frequency of the interference field and is due to the effective change in size of the pixel when rotating, constantly changing the sampling frequency.

The automated procedure consists of a sweep from 0° to 90° by the camera. The x and y part of the trajectory are mathematically complementary and complete in information about the Brillouin-zone folding, since the pixel lattice has a square symmetry. This explains why only a sweep of 90° is necessary to obtain all information. Then, of each real-space frame a fast Fourier transform is made after which a peak-finder (that works best if the center peak is filtered out) is used to find the alias frequencies. Hence, we are able to track the peaks, for any two-beam configuration. The peak finder [32] is not perfect, so many false data points are filtered out in the process later on, by setting a lower boundary to the peak values and cropping away the center peak.

Next, the full 180° signal f_{xm} is plotted and the model, as explained in chapter 2, is fitted to it using the SciPy DIRECT function [33], using the fact these curves are unique to one combination of sampling frequency (f_s) and spatial fringe frequency (f_{orig}). From this, the exact angle between the beams can be obtained by formula 2.6. In figure 4.4 it is shown how part of the trajectory can look like and how well the fitting goes, even when some

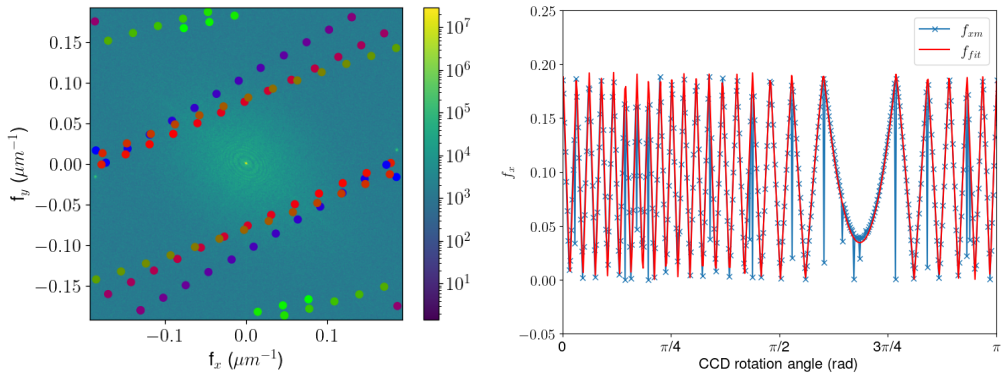

(a) ***(b)***

Figure 4.4: *The partial trajectory of an FFT-peak (a) and its derived x and y-components which are fitted to the model (b).*

data points are clearly false. The accuracy of this method can be tested by putting in different simulations of interfering beams that by definition have an angle between them and compare them to the measured output angles. In table 4.2 the six input angles are compared with the angle that followed from the analysis.

Input	**Fit**
90.6°	90.607°
90.0	89.956°
90.0°	89.990°
90.0°	89.990°
93.8°	94.178°
90.0°	90.236°

Table 4.2: *The comparison of input angles with the values resulting from the automated beam angle finding procedure of the numerically simulated experiment.*

Note, that two measurements have a much greater error than the other four, and that is due to the fact that in the fitting a small deviation from the correct location of the beam is present. This phenomenon is displayed in figure 4.5. From this it follows that the mean-squared error of our angle finding method is 0.03°, but can be even lower if one manually ensures that the fit overlaps completely with the data, by changing the bounds of f_{orig} in the fitting procedure, such that this error gets smaller.

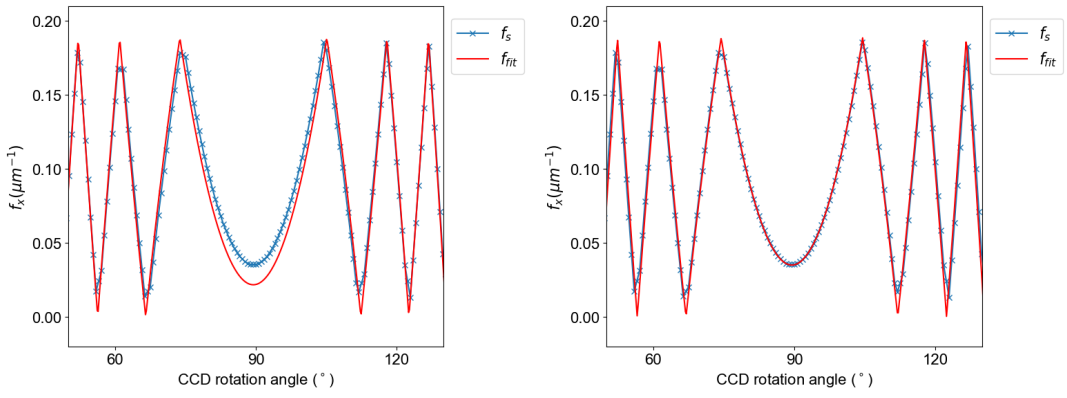

(a) ***(b)***

Figure 4.5: *A fit using SciPy's DIRECT method to obtain the measured frequency signal of a simulation with a small deviation (a) and a closer fit (b).*

Version of November 10, 2023– Created November 10, 2023 - 13:12

To conclude, this automated beam angle finding procedure is very precise, does not last more than ten minutes after measurement and is proven to be able to handle many different measurements. This robust method can now be used to observe how well-aligned the beams are after alignment with the reticle and if the configuration is within the range of achieving a homogeneous field.

4.2 Interferometric visibility of multiple superposed beams

Through the iterative process of tuning the angle of the beams and aligning them in such a way that their centers match on the CMOS-camera, we were able to image the field of interference of many beam combinations, knowing that this alignment was of the highest quality achieved so far. Hence, these measurements were analyzed and we investigated whether a homogeneous field of interference could be reached.

In figure 4.6 the real-space image of these four superposed beams is shown, next to its FFT. The attempt was to place the centers of the beams at the same location, but one of the beams ended up being a bit displaced. After all, the FFT maxima are in a good square and the 60° maxima of adjacent beams overlap, so this confirms again that alignment must be very close to the desired configuration.

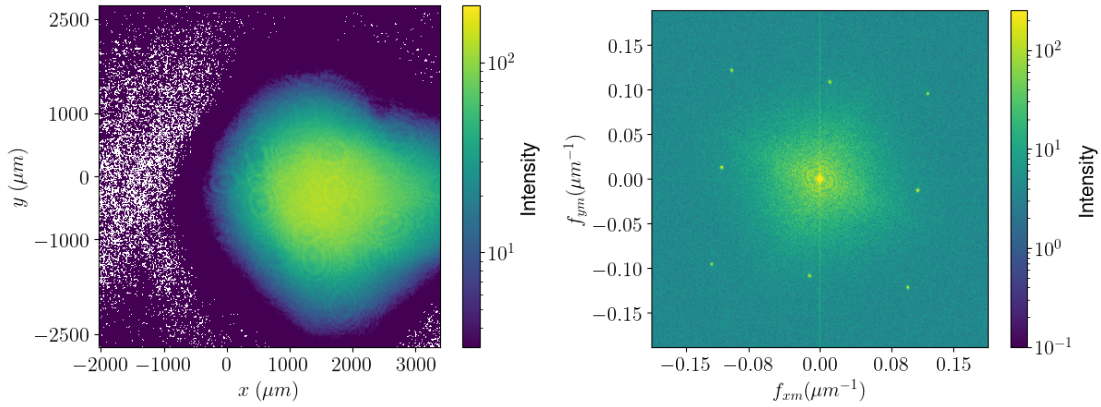

(a) ***(b)***

Figure 4.6: *The real-space (a) and the 2D fast fourier transform (b) of four superposed laser beams that were put in very good alignment with each other.*

Using the alignment methods described in the previous sections, the four beams could be put in good alignment, leading to the measured relative angles of table 4.3. While the measured beam angles of combinations A-B and C-D agree with the fact that their FFT peaks overlap, beam combinations B-C and A-D result in different measured angles while having overlapping FFT peaks in figure 4.6(b). This is due to the fact that the angle between two beams can only be measured if a CMOS camera sweep on two beams is made, due to the current peak finding algorithm. The

combination of a non-perfect peakfinder leading to a small deviation per measurement with the probability that the angle could have been altered slightly throughout the measurement day gives rise to this difference.

i, j	$\theta_{i,j}$
A-C	90.6°
B-D	90.6°
A-B	60.3°
B-C	60.4°
C-D	60.3°
A-D	60.5°

Table 4.3: *The relative angles between the four beams as obtained by the automated beam finding procedure. Following the previous section, their error is* 0.03°.

Using this configuration of the four beams, we can calculate the expected superchiral structure and this lattice can be confirmed to be existent with a small decrease of the superchiral area by 10% (namely from 21% to 19%). This is promising, but the interference pattern that still seems to be present will be investigated in the coming sections.

4.2.1 Polarized two-beam interference

The simplest experiment one can do to observe whether an interferometric visibility change can occur is by putting *two* beams deliberately in a maximally interfering superposition, i.e. paralellizing their polarization on the region of interference. When this is compared to the case where they are perpendicular, an interferometric visibility change must be detected. Now, this is quantified by the height of the FFT-peaks and for convenience the peak height will be displayed without a unit from now on, since it is essentially of the same kind as intensity and only the relative height matters. To be consistent throughout all experiments this unit was kept equal.

Two half-wave plates allow us to perform this polarization rotation and to get a better view of the experimental setup, figure 4.7 shows a schematic representation of the experiment. The blue arrows represent the polarization directions. In figure 4.8 the peak height for a sweep of 90° is shown for both cases. Both measurements seem to have a slight increase of the FFT peak height around -60°, although throughout the entire sweep there is much noise. This point corresponds to the minimum of the parabola

Version of November 10, 2023– Created November 10, 2023 - 13:12

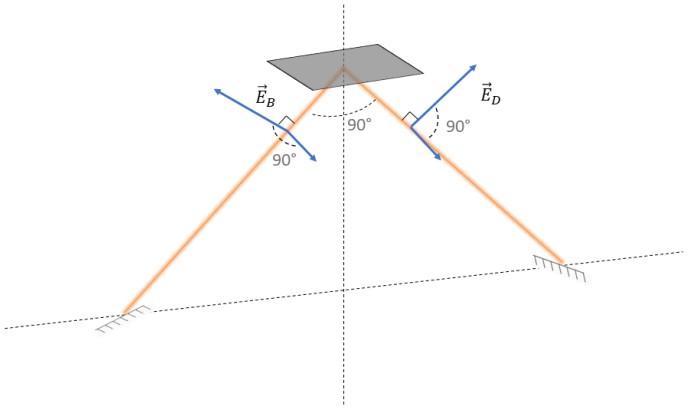

Figure 4.7: *A schematic view of the setup of the experiment where the black rectangle represents the CMOS camera. Two beams with a polarization in either perpendicular directions or parallel directions are superposed on the beam profiler.*

when measuring f_{xm}, meaning that this is in fact the point at which the pixels are parallelly aligned with the interference pattern. In the coming sections this point will be the gauge for the measurement and will be set as zero. The peaks of the two different measurements have clear different heights at this point, but it is not possible to say with how much. Still, they confirm the result from the simulations that around 0° a global maximum is expected.

The angle between the two beams is found to equal 90.7°, which already partially explains why the interference does not fully disappear when the polarizations are shifted to the theoretical orthogonal direction. Still, one would expect that interference decreases more, since from simulation it follows that this difference should be larger when these beams have such an angle – namely a factor 10^4 (figure 2.15) – which is more near a factor of 2 in the experimental case. This could also be due to other structures present at the CMOS camera (such as microlenses) which will be discussed later on.

To conclude, the 0° signal does disappear, so an indication of a interferometric visibility decrease is present. This follows from the fact that the most reliable measurement angle of the camera is when the pixels are aligned with the interference pattern.

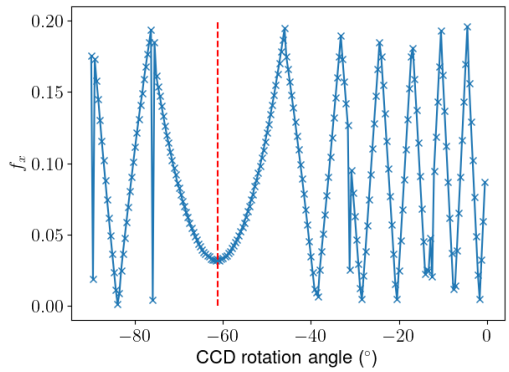

(a)

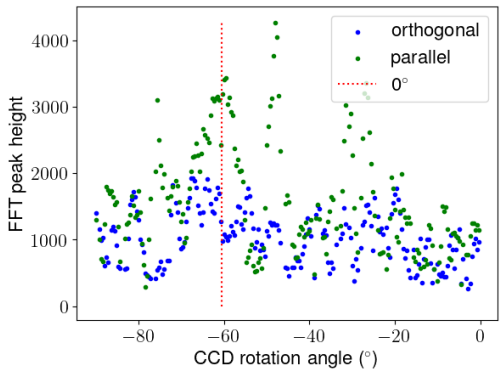

(b)

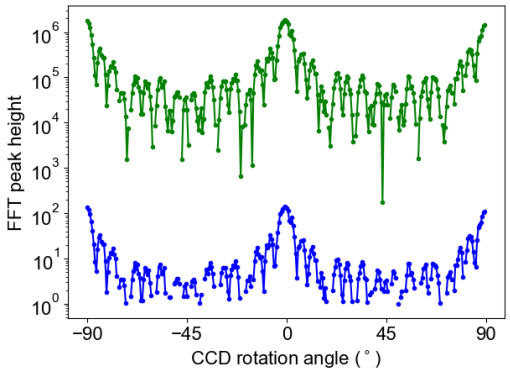

(c)

Figure 4.8: *A measurement of the (aliased) spatial frequency component f_x (a) to determine the beam angle ($\theta_{BD} = 90.7°$) and to determine the 0° point where pixels align with the interference pattern. (b) & (c) show the comparison of the height of the peaks in the experimental and the simulated FFT of two extreme cases: parallelly polarized and orthogonally polarized.*

4.2.2 The influence of alignment errors

In order to investigate what the effect is of good laser alignment on visible interference, two 90° sweeps were performed on well and worse aligned opposing beams, namely B and D. The angles between these beams were found to equal respectively 90.6° and 93.8° and their polarization was chosen to be (approximately) orthogonal. In figure 4.9 the height of the FFT peaks is plotted versus the rotation angle of the CMOS camera, with 0° defined as the point where the pixels are aligned with the interference pattern, which can be found via the analysis of the measured spatial frequencies at the FFT.

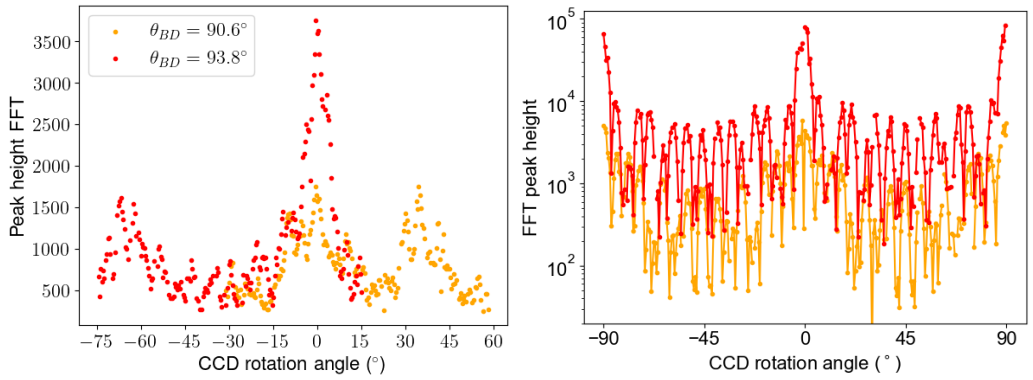

(a) ***(b)***

Figure 4.9: *The experimental (a) and simulated (b) interference of two beams with (almost) perpendicular polarization and a certain angle between the beams θ_{BD}.*

As expected, around 0° the height of the FFT peaks decreases with worse alignment. In simulation, this is confirmed, but this difference equals one order of magnitude whereas in experiment this factor approximately equals 2.

Again, around 30° and -60° two (presumably equivalent) extra smaller peaks are observed, which were also seen in the previous intensity experiment. Since the simulations do not predict such a peak, some effect that is not incorporated in the simulation should be the cause of this. This can for example be caused by some optimal angle at which the pixels collect most light and even the microlenses on the pixels could play a role in this.

4.2.3 Pixel structure and microlenses

Yet, the most striking part of all these previous measurements is that there seems to be a lower bound to how much the interference can decrease. This is a sign that interference does not really become homogeneous. Since lasers are a rather perfect monochromatic and polarized light source, the reason of this happening must lay in either the alignment (which is near-perfect) or in the measurement technique.

It turns out that on the used CMOS camera microlenses are present. In general, these are used to correct for the fact that pixels collect more light from the direction of the normal axis than from the edges, making the view of the pixel broader than the size of the pixel. In this experiment however, these microlenses are potentially disturbing the experiment. In figure 4.10

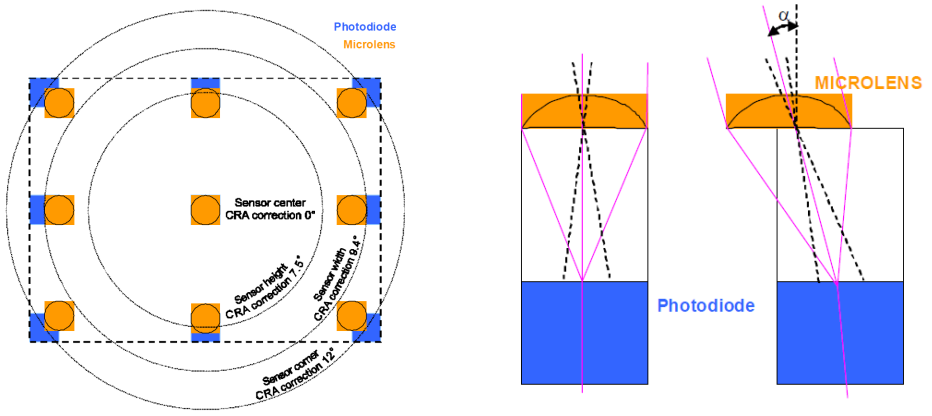

Figure 4.10: *Microlenses on the pixels are shifted radially according to the Chief Ray Angle method (a) which makes the field of view of the camera broader whilst keeping an equal intensity for each direction. The microlenses modify the direction and focus of the two beams (b), hence modifying the interference upon measurement.*

it is shown that the lenses cause a displacement determined by their radial distance from the center and how incident light from different angles is collected at the pixel area. We do not know the exact radius of curvature of the lenses and the distance they have with respect to the pixels, since this is not published by the company. It is likely that the microlenses modify the local wave direction and the polarization such that interference reappears.

The extra signal that arises in some measurements around 35° could perhaps also be due to the microlenses, but it is more likely that it is due to the shape of the pixels. Namely, the pixels are partially (sometimes up to 70%) covered with support transistors, which are relatively opaque to visible light, hence also for the 632.8 nm wavelength beam. This can alter the shape of the photodiode inside the pixel, altering the rotational symmetry of the measurements by the means of the amount of collected light, while keeping the pixel distance equal. Therefore, the f_{xm} and f_{ym} remain trivially related by $\theta_{\text{CMOS}} + 90°$ due to the square lattice configuration, but the height of the FFT peaks can show extra dependencies on the rotation angle of the CMOS camera due to the shape of a single pixel. In combination with the microlens shifting, which is dependent on the radial distance of a pixel from the center, some effects could become even more pronounced. The diagonal of the rectangular pixel array makes an angle of $\arctan(\frac{1024}{1280}) = 38.7°$ with the axis, meaning that at this angle some ef-

fects could become more pronounced. The exact coverage and shape of the pixel remains unknown, but it is our hypothesis that this is the main cause of the extra FFT peak signals arising at some camera rotation angles.

Chapter 5

Conclusions & outlook

In this research it is shown that it is experimentally possible to achieve a subpixel superresolution by a rotating camera. An analysis of the FFT peaks enabled us fit the data to a model and find the corresponding original fringe period, which was at first irretrievable due to aliasing. In experiment, this could be used to determine the angle between two interfering beams, via a newly automated and very quick FFT peak analysis. The combination of this method, the theoretical knowledge of beam interference and the ability to rotate the camera resulted in a beam angle determination accuracy of $\sigma_\theta = 0.03^\circ$. This achievement could possibly also be of importance when measuring other subpixel structures.

Most importantly, this new method resulted in knowledge about the quality of the manual beam alignment method with a reticle. Namely, aiming at the perfect angle of 90° between opposing beams and 60° between adjacent beams, which is required to produce superchiral fields, the reticle method in combination with the ability to observe the FFT in real time resulted in a near-perfect alignment of the beams. This configuration theoretically has a near-zero amount of interferometric visibility. The superchirality lattice should largely remain intact at this obtained quality of alignment, so a method to measure this can be developed. The bright superchirality lattice would be the first of its kind and can possibly have applications in fabrication or detection of chiral nanostructures.

Two simulation methods were performed, of which the one with integration on the pixels resulted in realistic aliasing while rotating the pixel grid. This provided insights about the influence of the rotational angle with respect to the interference fringes on the visibility of the interference, from

which it is concluded that alignment of the pixels with the interference pattern results in an increased FFT peak height. We experimentally investigated near-perfect two-beam interference and how the FFT peak height (and thus the interferometric visibility) changes when altering the polarization or the alignment of the laser beams. From these experiments it can be concluded that if the CMOS camera is aligned with the interference pattern, the most reliable information on interferometric visibility can be obtained.

For orthogonally polarized beams, we did observe only a weak reduction of the interference pattern - we attribute this to the microlens array of the CMOS camera. The microlenses on the pixel array alter the net direction of the beams before reaching the photodiode, hence altering the electric field at the point of detection. In the future, similar measurements on CMOS without microlenses could be performed to investigate whether an improvement is possible. Around 30° another FFT peak signal was found, of which the cause remains unknown but the expectation is that it is caused by the shape of the photodiodes in the pixel being not perfectly symmetric.

Outlook

We have identified several interesting future research directions, in particular on the influence of microlenses, the ability to measure superchirality and a study of the four-beam interference. The presumed asymmetry of the photodiode at the pixel should be studied, too. The beam-angle finding procedure could possibly in the future be improved to automatically measure the angles between the ensemble of four beams at once, making a measurement of all beam combinations separately unnecessary.

Since this method proved to be very robust, applications in other fields could become reality too. The procedure can easily be adjusted to different pixel sizes and wavelengths so a more general determination of angles can be used to determine relative locations of beam sources.

This setup could also become of use in microscopy, where in some fields an interference pattern on the studied sample is not desired. At the region of interference, the electric field has an angle with the sample, but the net k-vector of the incoming light is normal to the sample. This is a new configuration that cannot be reproduced by a single beam.

Additionally, starting from a homogeneous interference pattern, the current setup is very sensitive to small angular displacements of the four

beams. This is because the simulations indicate that at the point of no interference, small increases of the amount of interference have the largest effect on the height of the FFT peaks. This makes this apparatus potentially very sensitive, and multiple-beam interference could hence open up new tri- and multilateration possibilities.

Furthermore, if the 3D structure of the $\tilde{\mathbf{E}}$ and $\tilde{\mathbf{H}}$ field at the region of interference could be experimentally imaged, this would mean final confirmation on whether the theoretical superchiral lattice structure is present. Until that time, one could think of indirect ways to measure the (super-)chiral structure of the light, for example by shining it onto an array of chiral molecules and imaging the transmissivity of the light. Using the chiral photoresist production method applied by He et al. [34], one could also fabricate a lattice with alternating chiralities of the photoresist, and measure its chirality by an existing method. Since the structure is at the scale of one wavelength, using a laser with a larger wavelength should be considered. This could also reduce aliasing effects.

Overall, it is shown in this thesis that the combination of aliased FFTs and interference of multiple laser beams can be very powerful en has lead to important insights. Hopefully in the future both superchirality and the pixel superresolution can play an important role in science and industry.

Acknowledgements

First, I'd like to thank my supervisor Wolfgang who has helped me with everything necessary to establish this thesis and supplied me with the necessary background to start with the project. I also liked the talks about other topics we had, they were interesting discussions. I also thank Michel Orrit for the very good and comprehensive feedback on the thesis.

It was a good choice to join the Quantum Optics group, I have learned a lot about working precisely and doing a more solistic research. I quickly found out that every group has different styles in how to do scientific research best and have again learned more about what working styles, both individual as in a team, suit me best. Next master students I would like to advise to really dive deep into the matter, whether you have a PhD student as supervisor or not. It is worth it not only because of the physics, but it also helps finding your way into the research.

Also Petr, Matteo, Kirsten, Mio, Thomas, Thom, Yasmin and Lisa must be acknowledged for their warm presence in the group. I really liked the 'gezelligheid' at the ninth floor and the many things we did together, such as the festivities and dinners we had.

I would also like to thank Coen (and Jan), who got me nicely distracted from the research by asking me to join his team at VJK. And all other committees and responsibilities like CASSA, the RvC, het Grote Blad, the padrigaal and the bundelcommissie must be noted as a rich – and a busy schedule enhancing – addition to my life too.

Eva, you were my best support in times where motivation was lower, new problems arose or the research in combination with all other things was a bit too hard to manage. Thanks also to Luc and Geert, who were very welcome lunch and coffee partners.

Appendix A

An additional beam intensity experiment

Figure A.1 shows an experimental investigation of how a difference in beam intensity affects the FFT peak for two nearly orthogonally polarized beams at an angle of 90.56° with each other. When the intensity of one of the beams is decreased, the signal around 0° for the FFT peaks gets more pronounced with a factor of approximately 2. At other angles there seems to be no difference.

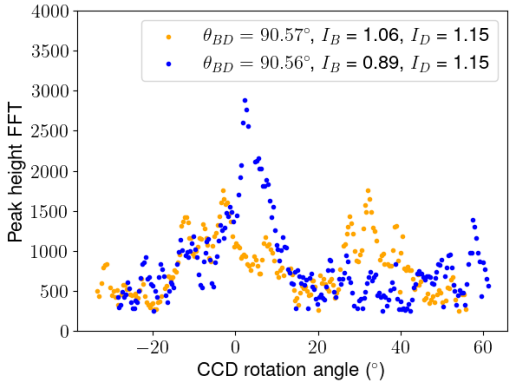

Figure A.1: *A measurement of two beams with good alignment but with differing intensity ratios.*

Around 30° an extra peak appears in one of the two measurements. The other measurement seemingly has a peak arising at 60° but this remains unsure. Most likely, this is due to the fact that the individual CMOS camera pixels are not fully 90° rotationally symmetric.

Bibliography

[1] T. Young, "I. the bakerian lecture. experiments and calculations relative to physical optics", Philosophical transactions of the Royal Society of London, 1–16 (1804) (cited on page 5).

[2] M. Saxena, G. Eluru, and S. S. Gorthi, "Structured illumination microscopy", Advances in Optics and Photonics **7**, 241–275 (2015) (cited on page 5).

[3] V. A. Barr and S. C. Bunnell, "Interference reflection microscopy", Current protocols in cell biology **45**, 4–23 (2009) (cited on page 5).

[4] M. Neil, R Juškaitis, and T Wilson, "Real time 3d fluorescence microscopy by two beam interference illumination", Optics communications **153**, 1–4 (1998) (cited on page 5).

[5] N. D. Lai, W. P. Liang, J. H. Lin, C. C. Hsu, and C. H. Lin, "Fabrication of two-and three-dimensional periodic structures by multi-exposure of two-beam interference technique", Optics Express **13**, 9605–9611 (2005) (cited on page 5).

[6] A. Fernandez and D. W. Phillion, "Effects of phase shifts on four-beam interference patterns", Applied optics **37**, 473–478 (1998) (cited on page 5).

[7] K. Van Kruining, R. Cameron, and J. Götte, "Superpositions of up to six plane waves without electric-field interference", Optica **5**, 1091–1098 (2018) (cited on pages 5, 8–11).

[8] Y. Tang and A. E. Cohen, "Optical chirality and its interaction with matter", Physical review letters **104**, 163901 (2010) (cited on page 5).

[9] Y. Tang and A. E. Cohen, "Enhanced enantioselectivity in excitation of chiral molecules by superchiral light", Science **332**, 333–336 (2011) (cited on page 5).

[10] C. Kelly, L. Khosravi Khorashad, N. Gadegaard, L. D. Barron, A. O. Govorov, A. S. Karimullah, and M. Kadodwala, "Controlling metamaterial transparency with superchiral fields", Acs Photonics **5**, 535–543 (2018) (cited on page 6).

[11] R. Tullius, G. W. Platt, L. Khosravi Khorashad, N. Gadegaard, A. J. Lapthorn, V. M. Rotello, G. Cooke, L. D. Barron, A. O. Govorov, A. S. Karimullah, et al., "Superchiral plasmonic phase sensitivity for fingerprinting of protein interface structure", ACS nano **11**, 12049–12056 (2017) (cited on page 6).

[12] E. Hendry, T Carpy, J Johnston, M Popland, R. Mikhaylovskiy, A. Lapthorn, S. Kelly, L. Barron, N Gadegaard, and M. Kadodwala, "Ultrasensitive detection and characterization of biomolecules using superchiral fields", Nature nanotechnology **5**, 783–787 (2010) (cited on page 6).

[13] T. Jia, B. Li, Z. Zhang, B. Gu, and G. Rui, "Superchirality induced enhanced circular dichroism spectroscopy via multi-beam superposition", Results in Physics **52**, 106857 (2023) (cited on page 6).

[14] S. Adhikari and M. Orrit, "Optically probing the chirality of single plasmonic nanostructures and of single molecules: potential and obstacles", ACS photonics **9**, 3486–3497 (2022) (cited on page 6).

[15] L. Wan, T. Yu, D. Zhao, and W. Löffler, "Pixel superresolution interference pattern sensing via the aliasing effect for laser frequency metrology", Laser Photonics Reviews **17**, `10.1002/lpor.202200994` (2023) (cited on pages 6, 16).

[16] G. M. Burrow and T. K. Gaylord, "Multi-beam interference advances and applications: nano-electronics, photonic crystals, metamaterials, subwavelength structures, optical trapping, and biomedical structures", Micromachines **2**, 221–257 (2011) (cited on page 8).

[17] Y. Tang and A. E. Cohen, "Optical chirality and its interaction with matter", Physical review letters **104**, 163901 (2010) (cited on page 9).

[18] D. M. Lipkin, "Existence of a new conservation law in electromagnetic theory", Journal of Mathematical Physics **5**, 696–700 (1964) (cited on page 10).

[19] J. L. Trueba and A. F. Ranada, "The electromagnetic helicity", European Journal of Physics **17**, 141 (1996) (cited on page 10).

[20] C. R. Harris, K. J. Millman, S. J. van der Walt, R. Gommers, P. Virtanen, D. Cournapeau, E. Wieser, J. Taylor, S. Berg, N. J. Smith, R. Kern, M. Picus, S. Hoyer, M. H. van Kerkwijk, M. Brett, A. Haldane, J. F. del Río, M. Wiebe, P. Peterson, P. Gérard-Marchant, K. Sheppard, T. Reddy, W. Weckesser, H. Abbasi, C. Gohlke, and T. E. Oliphant, "Array programming with NumPy", Nature **585**, 357–362 (2020) (cited on pages 12, 16).

[21] J. Kaiser and R. Schafer, "On the use of the i0-sinh window for spectrum analysis", IEEE Transactions on Acoustics, Speech, and Signal Processing **28**, 105–107 (1980) (cited on page 14).

[22] W. R. Inc., *Mathematica, Version 13.3*, Champaign, IL, 2023 (cited on pages 19–20).

[23] T. M. Inc., *Matlab version: 9.13.0 (r2022b)*, Natick, Massachusetts, United States, 2022 (cited on pages 19–20).

[24] *Helium-neon laser heads 1100 series*, JDS Uniphase, (2005) https://www.utwente.nl/en/tnw/slt/documentation/Equipment/Lasers/helium_neonlaserheads_1100s.pdf (cited on pages 25, 27).

[25] *Glan-taylor calcite polarizers*, https://www.thorlabs.com/newgrouppage9.cfm?objectgroup_id=816&pn=GT5-A (cited on pages 26–27).

[26] *Cincam cmos technical data*, CINOGY Technologies, http://www.cinogy.com/CinCam_CMOS_DataSheet.pdf (cited on page 27).

[27] *Integrated 3-axis motion controller/driver*, (2017) https://www.newport.com/medias/sys_master/images/images/hda/h3e/9117547069470/ESP301-User-s-Manual.pdf (cited on page 27).

[28] *Non-polarizing cube beamsplitters (400 - 700 nm)*, https://www.thorlabs.com/newgrouppage9.cfm?objectgroup_id=754 (cited on page 27).

[29] *Digital handheld optical power and energy meter console*, https://www.thorlabs.com/newgrouppage9.cfm?objectgroup_id=3341 (cited on page 27).

[30] *Polymer zero-order half-wave plates*, https://www.thorlabs.com/newgrouppage9.cfm?objectgroup_ID=7054 (cited on page 27).

[31] *E-663 3-channel piezo amplifier*, https://www.pi-usa.us/en/products/piezo-drivers-controllers-power-supplies-high-voltage-amplifiers/e-663-three-channel-piezo-driver-601800#specification (cited on page 27).

[32] S. Van der Walt, J. L. Schönberger, J. Nunez-Iglesias, F. Boulogne, J. D. Warner, N. Yager, E. Gouillart, and T. Yu, "Scikit-image: image processing in python", PeerJ **2**, e453 (2014) (cited on page 33).

[33] P. Virtanen, R. Gommers, T. E. Oliphant, M. Haberland, T. Reddy, D. Cournapeau, E. Burovski, P. Peterson, W. Weckesser, J. Bright, S. J. van der Walt, M. Brett, J. Wilson, K. J. Millman, N. Mayorov, A. R. J. Nelson, E. Jones, R. Kern, E. Larson, C. J. Carey, İ. Polat, Y. Feng, E. W. Moore, J. VanderPlas, D. Laxalde, J. Perktold, R. Cimrman, I. Henriksen, E. A. Quintero, C. R. Harris, A. M. Archibald, A. H. Ribeiro, F. Pedregosa, P. van Mulbregt, and SciPy 1.0 Contributors, "SciPy 1.0: Fundamental Algorithms for Scientific Computing in Python", Nature Methods **17**, 261–272 (2020) (cited on page 33).

[34] C. He, G. Yang, Y. Kuai, S. Shan, L. Yang, J. Hu, D. Zhang, Q. Zhang, and G. Zou, "Dissymmetry enhancement in enantioselective synthesis of helical polydiacetylene by application of superchiral light", Nature Communications **9**, 5117 (2018) (cited on page 45).